



Markus Gößler BSc

# Hydrogen Storage and Actuation Properties of Nanoporous Palladium Prepared by Dealloying

Master's Thesis

to achieve the university degree of

Diplom-Ingenieur

Master's Degree Programme: Advanced Materials Science

submitted to

**Graz University of Technology**

Supervisor

Univ.-Prof. Dipl.-Phys. Dr.rer.nat. Roland Würschum  
Institute of Materials Physics

Co-supervisor

Dipl.-Ing. Dr.techn. Eva-Maria Steyskal  
Institute of Materials Physics

Graz, May 2017



# Affidavit

I declare that I have authored this thesis independently, that I have not used other than the declared sources/resources, and that I have explicitly marked all material which has been quoted either literally or by content from the used sources.

---

Date

---

Signature



# Abstract

Within the scope of this thesis nanoporous palladium samples were produced by dealloying and studied with respect to their hydrogen-loading behaviour. The palladium-hydrogen system has been an extensively studied model for hydrogen storage in metals over the last decades. The ability of palladium to absorb hydrogen atoms in its bulk is a clear distinction from other platinum group metals, which are only capable of adsorbing hydrogen on the surface. Nanoporous palladium samples, as prepared in this thesis, exhibit high surface-to-volume ratios and allow fast hydrogen sorption. In the scope of this work nanoporous palladium samples were prepared via electrochemical dealloying, a selective dissolution process which etches a less noble element out of a precursor alloy. Four different compositions of cobalt-palladium alloys (CoPd88/12at%, 80/20at%, 75/25at%, 70/30at%) were prepared as master alloys. Nanoporous samples were placed in an electrochemical cell as electrodes to investigate hydrogen sorption electrochemically, while in-situ dilatometric measurements could be conducted using a special experimental setup. The electrochemical measurement techniques of cyclic voltammetry and chronoamperometry were applied in different electrolytes such as KOH, KCl, H<sub>2</sub>SO<sub>4</sub> and HClO<sub>4</sub> solution. The goal of this thesis was the systematic study of hydrogen sorption and the corresponding actuation behaviour in nanoporous palladium with respect to master alloy composition, applied voltage and used electrolyte. Key parameters of actuator materials, as electrocapillary coupling coefficients and strain amplitude, were determined for nanoporous palladium. A maximum reversible expansion of more than 3% could be attained during hydrogen loading of nanoporous palladium in KOH. Unexpected irreversible length changes occurred during potentiostatic loading at strongly cathodic potentials and in acidic electrolytes. Those could be explained considering chemical reactions in the electrolytes, the hydrogen sorption kinetics as well as a strain rate dependence of the mechanical yield strength at low potentials.



# Kurzfassung

Im Rahmen dieser Arbeit wurden nanoporöse Palladiumproben durch Dealloying hergestellt und hinsichtlich ihres Verhaltens bei Wasserstoffbeladung untersucht. Das Palladium-Wasserstoff System war in den letzten Jahrzehnten ein wichtiges Modellsystem um die Wasserstoffspeicherung in Metallen zu untersuchen. Die Fähigkeit, Wasserstoff nicht nur an der Oberfläche zu adsorbieren, sondern in das Metallgitter interstitiell aufzunehmen, unterscheidet Palladium von anderen Übergangsmetallen derselben Hauptgruppe. Nanoporöse Palladiumproben, wie sie in dieser Arbeit hergestellt wurden, weisen hohe spezifische Oberflächen auf, welche eine schnelle Wasserstoffaufnahme begünstigen. Die nanoporösen Palladiumproben in dieser Arbeit wurden durch elektrochemisches Dealloying hergestellt. Darunter versteht man einen selektiven Ätzprozess, welcher das unedlere Metall aus einer Legierung löst. Vier verschiedene Zusammensetzungen von Kobalt-Palladium Legierungen wurden als Ausgangslegierung für den Dealloyingprozess hergestellt (CoPd88/12at%, 80/20at%, 75/25at%, 70/30at%). Die resultierenden nanoporösen Proben wurden als Elektroden in einer elektrochemischen Zelle verwendet, um den Wasserstoffeinbau zu untersuchen, während in-situ Längenänderungen durch einen speziellen Versuchsaufbau gemessen werden konnten. Die elektrochemischen Techniken der Zyklovoltammetrie und der Chronoamperometrie wurden in verschiedenen Elektrolyten, wie KOH, KCl, H<sub>2</sub>SO<sub>4</sub> und HClO<sub>4</sub> verwendet. Das Ziel dieser Arbeit war eine systematische Untersuchung der Wasserstoffspeicherung und der damit verbundenen Aktuation in nanoporösem Palladium hinsichtlich Ausgangslegierung, Elektrolyt und angelegter Spannung. Charakteristische Parameter für Aktuormaterialien, wie das Verhältnis Dehnung-zu-Ladung und die Dehnungsamplitude, wurden bestimmt. Eine maximale, reversible Ausdehnung von 3% konnte bei potentiostatischer Wasserstoffbeladung in KOH erreicht werden. Irreversible Längenänderungen wurden bei stark negativen Ladespannungen und bei Messungen in Säure festgestellt. Diese konnten durch chemische Reaktionen von Palladium mit dem Elektrolyten, kinetische Überlegungen, sowie der Abhängigkeit der mechanischen Eigenschaften von der Ausdehnungsgeschwindigkeit erklärt werden.



# Contents

<b>1</b>	<b>Introduction</b>	<b>1</b>
<b>2</b>	<b>Fundamentals</b>	<b>3</b>
2.1	Electrochemistry . . . . .	3
2.2	Dealloying . . . . .	8
2.3	The Palladium-Hydrogen System . . . . .	10
2.4	Chemical Reactions of Palladium . . . . .	12
<b>3</b>	<b>Experimental</b>	<b>14</b>
3.1	Alloy Fabrication . . . . .	14
3.2	Electrochemistry . . . . .	15
<b>4</b>	<b>Results</b>	<b>20</b>
4.1	Dealloying . . . . .	20
4.2	CVs in Different Electrolytes . . . . .	22
4.3	Hydrogen Storage in Nanoporous Palladium - Cyclic Voltammetric Studies . . . . .	24
4.4	Hydrogen Storage in Nanoporous Palladium - Chronoamperometric Studies . . . . .	26
4.5	Cyclic Voltammetry in the Hydrogen Regime . . . . .	33
4.6	Surface Area Determination . . . . .	35
4.7	Length Changes in Acidic and Neutral Electrolytes . . . . .	41
4.8	Scanning Electron Microscopy . . . . .	44
<b>5</b>	<b>Discussion</b>	<b>47</b>
5.1	The Dealloying Process . . . . .	47
5.2	Potential Dependence of Hydrogen Concentrations - Palladium Hydride Phases . . . . .	50
5.3	Quantitative Evaluation of Actuation . . . . .	51
5.4	Anomalous Behaviour of Samples from Alloy D . . . . .	56
5.5	Palladium Electrodissolution and Irreversible Strain . . . . .	59
5.6	Correction for the Irreversible Strain . . . . .	66
5.7	Nanoporous Palladium as Energy Storage Medium . . . . .	69
<b>6</b>	<b>Conclusion</b>	<b>71</b>



# Chapter 1

## Introduction

In the late 1980s nanoporous materials received first attention in the scientific community as functional structures with various possible applications. Since then interest in nanoporous materials has been growing steadily. Today multiple techniques for the formation of nanoporous materials are available. The spectrum ranges from compaction of nanoparticles, being a straightforward and easily accessible technique, to more sophisticated approaches such as inverse colloidal crystals, liquid crystal templating and dealloying, the preferred technique in this work<sup>[1]</sup>.

Nanoporous structures are characterised by a high surface-to-volume-ratio and a high fraction of available crystallographic sites with low coordination numbers. This implies an enhanced chemical activity, as many chemical reactions are restricted to phase boundaries or interfaces. Those features raised interest from various scientific fields, but as the most prominent application catalysis deserves special mention. The associated lowering of the activation energy can be exploited to increase the yield of many synthesis reactions. Understandably common catalyst materials such as platinum and palladium were amongst the first nanoporous structures to be produced and still belong to the best-characterised ones today.

Due to the ability of palladium to form alloys with atomic hydrogen, which clearly distinguishes it from platinum, a great field of additional potential applications opened up. Besides catalysis, palladium could find use as actuator material<sup>[2-4]</sup>, solid state hydrogen storage<sup>[5,6]</sup>, hydrogen sensor<sup>[5]</sup> or even as high-temperature superconductor in its hydrided form<sup>[7,8]</sup>. Nanoporous palladium fabricated by dealloying consists of a network structure with ligaments in the range of 5-20 nm<sup>[9]</sup>.

This complex structures in general show enhanced mechanical yield strengths compared to their bulk counterparts<sup>[10]</sup>. In the case of nanoporous palladium its capability of absorbing hydrogen makes the evolution of generic mechanical properties difficult to predict. In the present thesis a certain amount of discussion is dedicated to this topic and a new approach of strain-rate sensitive mechanical properties during the hydride phase transition will be introduced.

The overall aim of this thesis is to provide further insight in both hydrogen storage in nanoporous palladium and concomitant electrochemical actuation. Therefore in-situ dilatometry was conducted in parallel with electrochemical experiments. Both cyclovoltammetric and chronoamperometric measurements were performed in different electrolytes in order to control the amount of absorbed hydrogen and analyse the underlying mechanisms. This work is structured in four larger section: The first section is dedicated to the dealloying process itself, the second and third, being the core topics of this work, address the hydrogen storage in nanoporous palladium structures from different initial alloy stoichiometries and highlight differences and similarities. The last section will deal with palladium dissolution, the irreversible strain and their causes.

# Chapter 2

## Fundamentals

### 2.1 Electrochemistry

Electrochemistry deals with charge transfer reactions at electrode-electrolyte interfaces. Electrons act as mobile charge carriers in the usually solid electrodes, while ions are responsible for charge transport in the electrolyte. In the simplest case the electrolyte is a liquid ionic solution, while the electrode is a metal. Solid electrolytes have also found applications, e.g. in various battery systems<sup>[11]</sup>. In solid state physics charge transfer processes at semiconductor-metal interfaces can be described via the alignment of the Fermi-level and a resulting electronic band structure bending. Surely, band structures are properties of solids exclusively, but nonetheless a similar viewpoint of matching energy levels can be utilised to picture charge transfer processes at metal-electrolyte<sup>[12]</sup> or semiconductor-electrolyte interfaces<sup>[13]</sup>.

The built-in voltage at a junction of different metals in equilibrium equals their difference in work functions as it is exactly the energy needed to transfer an electron from one metal to the other. In electrochemistry an electron transfer to or from an electrolyte is always connected with a chemical reaction as there are no free electrons present in electrolyte solutions. Reactions involving a gain of electrons are called reductions while reactions involving a loss of electrons are called oxidations. As charge has to be conserved, oxidation and reduction always occur pairwise (redox reactions). A reaction which can act either as oxidative part or - when the direction of the reaction reverses - reductive part of a redox reaction is referred to as electrochemical half-reaction. For one specific electrochemical half-reaction a "work function" can be defined via the reaction's standard electrode potential  $E^0$ .  $E^0$  is the measured voltage difference of the half reaction to the standard hydrogen electrode (SHE). A negative

value of  $E^0$  indicates that the corresponding half-reaction is the oxidation in contact with the SHE. The underlying half-reaction of this electrode is  $2\text{H}_{(\text{aq})}^+ + 2\text{e}^- \rightleftharpoons \text{H}_2$ . The absolute electrode potential for the SHE amounts 4.5 V referred to vacuum level<sup>[12]</sup>. Measured values of  $E^0$  for many half-reactions are listed in tables in various chemistry textbooks. The electrode potentials in Volt can be converted into apparent work-functions by calculating the absolute electrode potential times the elementary charge.

In general electrochemistry focuses on characterisation of a certain electrode-electrolyte interface. The electrode of interest is called working electrode (WE). To make current pass through the system a second electrode - usually called counter electrode (CE) - is needed. In order to measure the potential at the working electrode a third electrode, the reference electrode (RE), which is unaffected by the current flow, is needed as point of reference. In principle the above mentioned SHE could be used as reference electrode but it is impractical because hydrogen gas is needed. In practice so-called secondary reference electrodes with a well-known constant electrode potential relative to the SHE (and thus a constant absolute electrode potential) are used, e.g. silver/silver chloride electrodes. The chemical reaction in Ag/AgCl half-cells can be written as:  $\text{Ag} + \text{Cl}^- \rightleftharpoons \text{AgCl} + \text{e}^-$ . As in the case with two metals in contact an outer voltage applied to the metal-electrolyte interface shifts the equilibrium and causes electron transfer within the metal or through the metal-electrolyte interface. Moreover, temperature and concentration of the oxidised or reduced species, respectively, affect electrochemical equilibria according to the Nernst equation (Eq.2.1).

$$E = E^0 + \frac{RT}{zF} \ln\left(\frac{a_{\text{Ox}}}{a_{\text{Red}}}\right) \quad (2.1)$$

$E$  denotes the effective electrode potential,  $E^0$  the standard electrode potential,  $R$  is the gas constant,  $T$  the temperature,  $z$  the number of transferred electrons,  $F$  is the Faraday constant, and  $a_{\text{Ox}}$  and  $a_{\text{Red}}$  are the activities of the oxidised and reduced species. If one of the two involved half-reactions (oxidation or reduction) includes  $\text{H}^+$ -ions the electrode potential becomes implicitly pH-dependent as can be easily seen from the Nernst equation. Due to the self-ionisation of water (autoprotolysis) a pH-dependent potential can also be measured in presence of  $\text{OH}^-$ -ions. A pH-independent reference electrode is the reversible hydrogen electrode (RHE), which measures the potential in the actual working electrode solution, not being separated by a salt bridge<sup>[14]</sup>. Potentials are commonly converted into values versus RHE, in order to enable comparability of measurements in different electrolytes. Electrode potentials of common reference electrodes are illustrated in Fig.2.1.

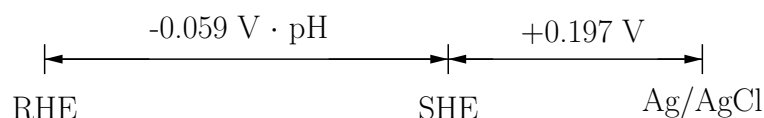


Figure 2.1: Schematic representation of different reference electrode potentials and their relation  
RHE..... reversible hydrogen electrode  
SHE..... standard hydrogen electrode  
Ag/AgCl... silver/silver chloride electrode

### 2.1.1 Cyclic voltammetry

Cyclic voltammetry (CV) is the most common electrochemical measurement method. The electrode current is tracked while varying the potential applied triangularly up and down using a potentiostat. The time dependence of the applied potential is illustrated in Fig.2.2. The starting voltage is usually set in a way such that the starting current is negligible. An increase in scan rate increases the voltammetric current (the peak currents are proportional to the square root of the scan rate<sup>[15]</sup>) and shifts the peak positions in scan direction, so to the right in the anodic cycle and to the left in the cathodic cycle.

A typical voltammogram recorded on a nanoporous palladium electrode is depicted in Fig.2.3. The curve is run through in clockwise direction. The upper branch is referred to as anodic half-cycle, while the lower branch is called cathodic half-cycle. The region ranging from 0.07 V to 0.5 V on the anodic half-cycle, characterised by a low overall current and no visible peaks, is attributed to the electrochemical double layer. In the double layer regime only capacitive charging at the electrode-electrolyte interface is responsible for the current flow, while no charge transfer across the interface takes place. At higher and lower potentials certain structures becomes apparent associated with higher currents. Each peak of this structure is characteristic for a certain chemical reaction.

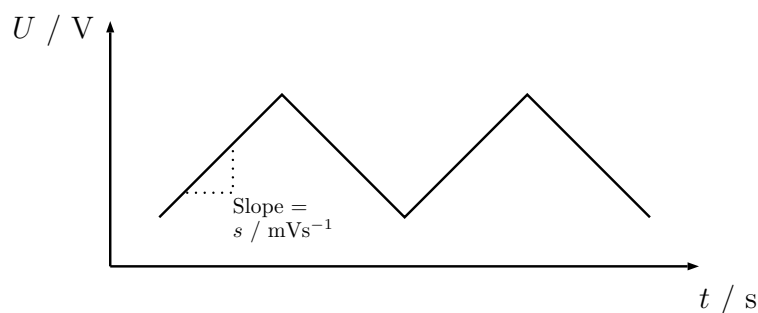


Figure 2.2: Voltage  $U$  as a function of time  $t$  for a typical cyclic voltammetry measurement,  $s$  denotes the scan rate

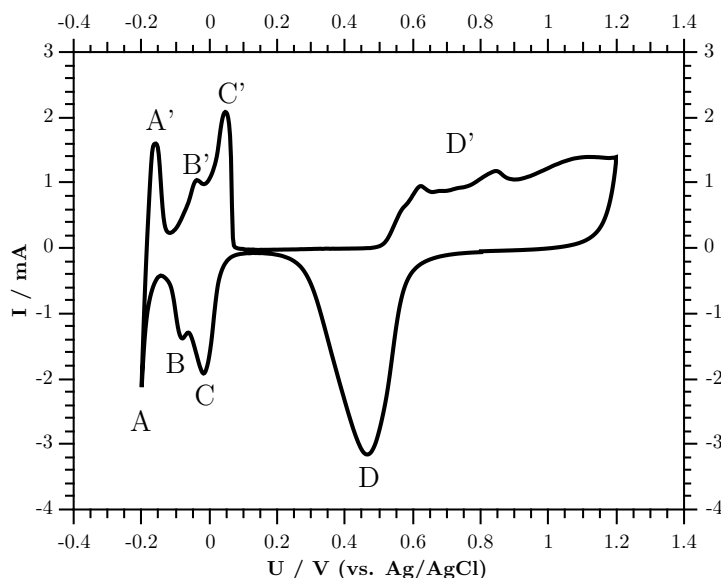


Figure 2.3: A typical CV measurement on a nanoporous palladium electrode in 0.5M  $\text{H}_2\text{SO}_4$  at a scan rate of  $0.1 \text{ mVs}^{-1}$ , exemplarily shown for sample B5, peaks are explained in the text

Reversible chemical reactions are defined by peaks shifted by no more than 57mV at 298K<sup>[15]</sup> in the cathodic (lower) and anodic (upper) half-cycle. It should be noted that the voltage scan rate has a strong influence on the reversibility of a reaction, as it ultimately changes the peak potentials. A typical case for a (scan-rate independent) irreversible chemical reaction on a palladium electrode is the formation of palladium oxide (see Sec.2.4). While the oxidation reaction takes place in a wide region at potentials above 0.5 V (peak D'), the corresponding reduction commences at much lower potentials below 0.65 V (peak D). At potentials higher than 1.25 V the process of oxygen evolution would dominate the current and cause a sharp increase in current.

Similarly, hydrogen evolution is responsible for the rise in (negative) current below -0.2 V. Multiple smaller cathodic peaks (A, B, C) can be identified in Fig.2.3, which are associated to hydrogen adsorption on the ligament surface and hydrogen  $\alpha$ -phase absorption in the ligament bulk<sup>[3,16]</sup>. The corresponding desorption peaks are marked in the anodic half-cycle (A', B', C'). Exact assignment of the processes to distinct peaks is not consistent in literature and will therefore not be covered in this section. However, the presence of differently bound hydrogen species on the palladium surface/in the palladium bulk is clearly indicated by those different peaks. The actual shape of the voltammogram does also depend on the used electrolyte.

An interesting feature is present in cyclic voltammograms recorded on nanoporous samples after preceding dealloying. The initial CV cycle, exhibits a strong cathodic peak shifted to lower potential values compared with regular oxygen desorption of the consecutive cycles (see e.g. Fig.4.2). This is attributed to a strongly bound oxidised species which forms on the sample surface in a parasitic process during dealloying. This effect has to be considered, whenever the charge during the dealloying process is evaluated. This first voltammetric cycle on a freshly dealloyed sample will be referred to as "Stripping" in this work, as the primary oxide layer is removed from the sample surface in the cathodic half-cycle. Nanoporous platinum electrodes, prepared by dealloying, show the characteristic stripping peak in the voltammograms in a more pronounced form<sup>[17]</sup>.

### **2.1.2 Chronoamperometry**

Chronoamperometry is another commonly used technique in electrochemical experiments and is defined as applying a constant potential to the working electrode and measuring the resulting current as a function of time. The current measured in such an experiment consists of a capacitive charging current which decays exponentially and a contribution of Faradaic reactions<sup>[15]</sup>. Coupled reactions additionally alter the shape of the current curves. The resulting curves often resemble standard exponentially decaying charging curves known from commercial capacitors, but can also exhibit distinct features if Faradaic reactions take place. This type of measurement allows an easy determination of the converted charge via numerical integration of the current-time-curves. Chronoamperometric measurements at low potentials were used to determine the amount of hydrogen stored in the nanoporous palladium structures. One of the main advantages of this technique is that by choosing a suitable potential gas evolution reactions can be avoided, in contrast to chronopotentiometric measurements, where the constant current almost always has a contribution from gas formation.

### **2.1.3 In-situ dilatometry**

Standard dilatometric experiments are an established tool in materials physics to gain insight in the microstructure of various materials. Distinction of phases and determination of coefficients of thermal expansion are standard applications of this technique. Simultaneous electrochemical and dilatometric measurements allow detection of length changes associated with chemical reactions and assertions concerning reaction reversibility<sup>[4]</sup>. Besides, an assessment of the mechanical properties of brittle materials as nanoporous palladium is possible

with respect to electrolyte solution and applied potential<sup>[18]</sup>.

## 2.2 Dealloying

Nanoporous materials have increasingly gained interest over the last decades due to attractive anomalous features compared to their bulk counterparts. Both chemical and physical properties on the nanoscale can differ widely from bulk values, which can be used to alter materials for specific applications, e.g. catalysts<sup>[19]</sup>, ion conductors<sup>[20]</sup>, optical devices<sup>[21]</sup> or, as in the present work, for hydrogen storage media.

Different routes are available for the formation of nanoporous materials, e.g. inert gas condensation, powder compaction or dealloying, which was the preferred pathway in this work. The process of dealloying, or selective dissolution, is based on a simple concept. A (binary) alloy, consisting of differently noble metals (more precise: metals with different electrochemical standard potentials) is exposed to an etching agent, acid or alkaline solution, leading to the dissolution of one component, while enhancing the surface diffusivity of the other. The second process is especially important for the formation of nanoporous network structures, as a suppressed surface diffusivity leads to a subsequent passivation of the alloy surface, preventing further etching.

In Fig.2.4 the dealloying process is depicted schematically for different alloy compositions. Fig.2.4 (a) shows the case of a passivating surface due to an impeded surface diffusivity of palladium atoms at the electrode-electrolyte-interface. This is the case for Pd-Fe or Pd-Ni alloys as shown by Hakamada<sup>[22]</sup>. In the passivated state the alloy surface is exclusively covered with atoms of the more noble element. Fig.2.4 (b) illustrates the dealloying process for a Pd-Co alloy, leading to the formation of a nanoporous network structure. Palladium atoms can diffuse at the electrode-electrolyte interface, leading to the formation of noble element clusters. As a result, areas of the less noble element are exposed to the electrolyte, which enables a continuous etching process in Pd-Co alloys. The resulting nanostructure has a high surface-to-volume ratio and thus a large surface energy, which is energetically unfavourable.

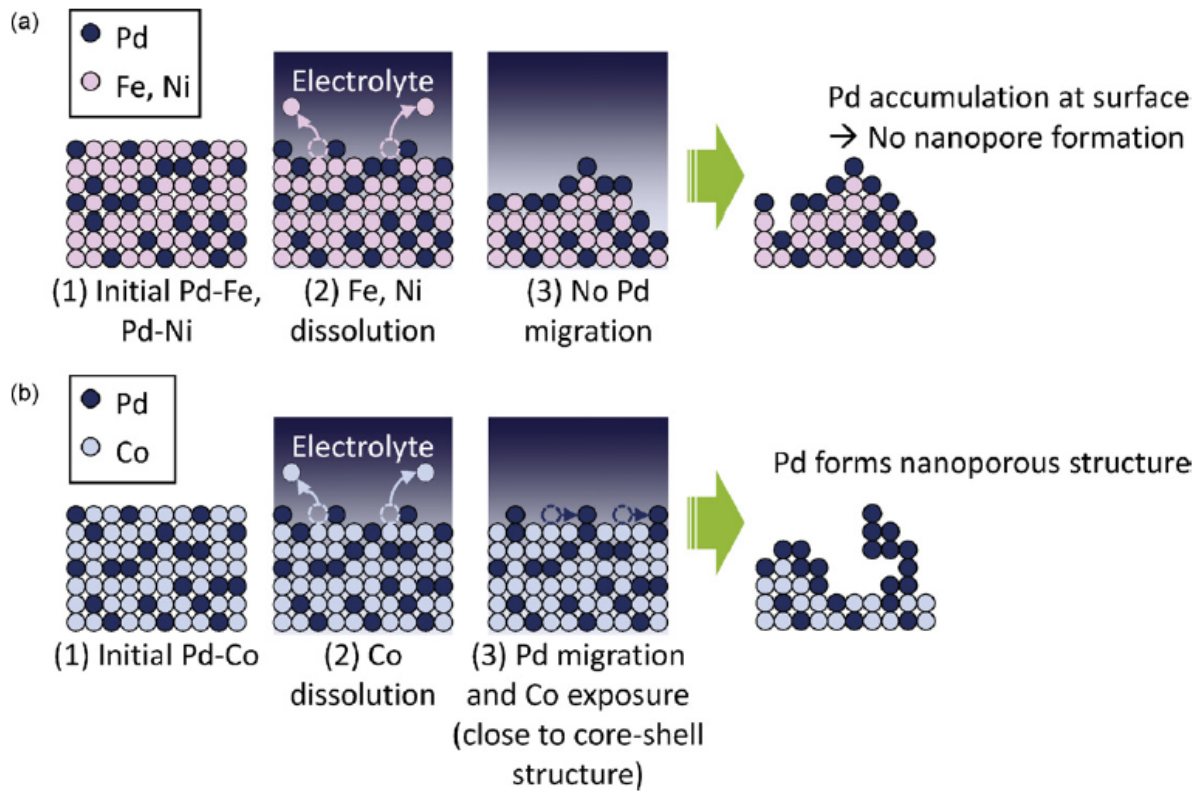


Figure 2.4: Schematic representation of the dealloying process, (a) for Pd-Fe and Pd-Ni alloys, (b) for a Pd-Co alloy, image reprinted from Hakamada et al.<sup>[22]</sup> with permission from Elsevier

High temperatures are a driving force to lower surface energy and coarsen the structure. After complete dissolution of the sacrificial element, the high surface diffusivity at the electrode-electrolyte interface is another factor influencing the coarsening of the nanostructure. This (often unwanted) effect can be prevented by rinsing the sample and removing the electrolyte in order to impede surface diffusion of the noble compound. Grain size does not change during the dealloying process. Grains comprise a certain volume of the nanoporous structure and include a lattice-coherent ligaments exclusively.

## 2.3 The Palladium-Hydrogen System

The central feature which distinguishes palladium from other noble metals such as platinum is its ability to absorb hydrogen into its bulk. This can lead to the formation of palladium-hydride alloys, depending on the hydrogen concentration. One aspect which is uncommon for metal hydrides<sup>[23]</sup> is that two different phases in palladium hydride have the same metal lattice structure. Palladium hosts solute hydrogen atoms on octahedral sites in its face-centered-cubic crystal lattice in both the solid solution ( $\alpha$ ) and the hydride ( $\beta$ ) phase. Thus, the limiting stoichiometry would be a sodium chloride crystal structure, when the hydrogen and palladium ratio H:Pd would be one. This stoichiometric compound has never been attained in practical experiments.

The phase diagram of palladium hydride is depicted in Fig.2.5. Two phases separated by a miscibility gap can be distinguished. At room temperature pure  $\alpha$ -phase is present below 0.03 H:Pd whereas pure  $\beta$ -phase commences at concentrations above 0.6 H:Pd. The lattice constant increases from 3.887 Å for pure palladium to 3.895 Å for the PdH  $\alpha$ -phase (maximum hydrogen concentration at 25° C) and amounts 4.025 Å in the pure  $\beta$ -phase (minimum hydrogen concentration at 25° C)<sup>[24]</sup>. This larger lattice constant in the  $\beta$ -phase lays the foundation for actuator applications of palladium hydride. For nanocrystalline palladium a narrowing of the miscibility gap in the phase diagram was reported<sup>[25]</sup>, which should also be considered in other nanostructured materials.

Different methods are available for hydrogen insertion into palladium. The classical method is the pressurisation of the metal with hydrogen gas, which allows to control the absorbed amount of hydrogen via the applied gas pressure. Another method utilises the electrochemical absorption of H<sup>+</sup>-ions into a palladium electrode. Thereby the charge flow can be used to control the hydrogen concentration in the lattice. A comparison of both methods can be found in the work of Jerkiewicz and Zolfaghari<sup>[26]</sup>. Gas-phase-loading usually involves the measurement of pressure-composition isotherms (PCIs), which allow an experimental distinction of palladium hydride phases. One interesting finding in those curves is a hysteresis loop considering loading and unloading processes<sup>[27]</sup>. The loading process generally requires higher pressures to attain a certain concentration than the unloading process. Thermodynamic models for the shape of those curves do exist and were adopted for palladium nanoparticles<sup>[28]</sup>.

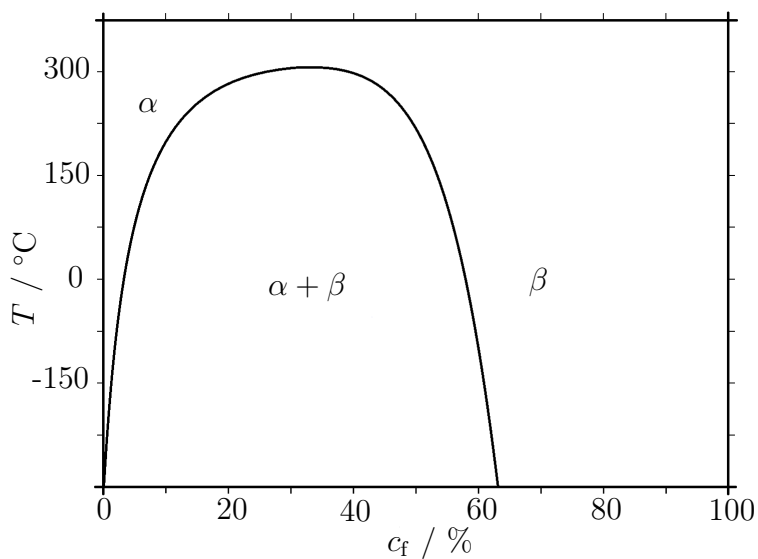


Figure 2.5: Schematic phase diagram of the palladium-hydrogen-system, temperature  $T$  over atomic ratio  $c_f$  of hydrogen and palladium (H:Pd)

In electrochemical measurements the distinction of palladium hydride phases is possible by measuring the hydrogen concentration as a function of applied polarisation potential (for experimental details see Sec.4.4). From a purely thermodynamic standpoint this type of plot is equivalent to the aforementioned pressure composition isotherms. A schematic plot of hydrogen concentration  $c_f$  versus potential can be found in Fig.2.6.

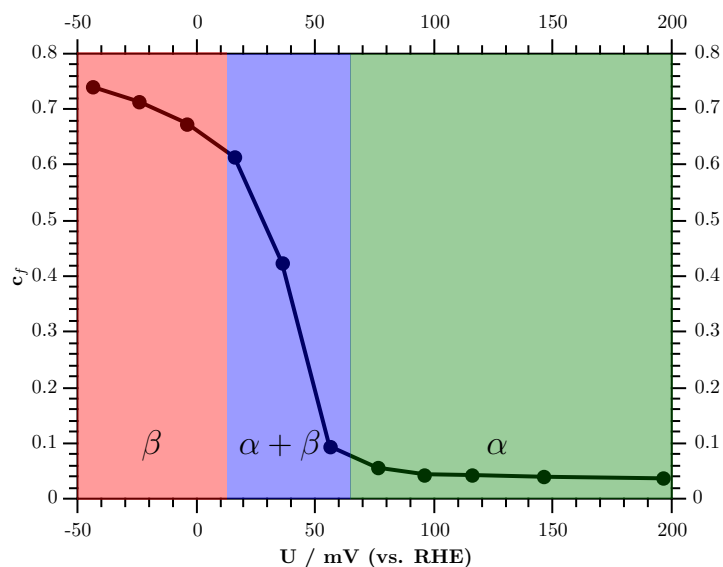


Figure 2.6: Schematic for the distinction of palladium hydride phases, atomic ratio of hydrogen and palladium  $c_f$  (H:Pd) versus polarisation potential  $U$ , different phases are indicated by coloured regions

## 2.4 Chemical Reactions of Palladium

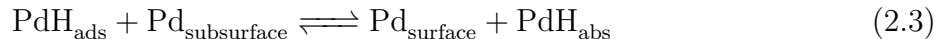
In this section the most important (electro-)chemical reactions of palladium shall be introduced in order to understand processes in different electrolytes occurring in later sections of this work.

### 2.4.1 Palladium Hydride Formation

Electrochemical hydrogen absorption in palladium is the central reaction investigated in this work. The mechanism of hydrogen absorption consists of two steps. The first involves hydrogen adsorption on the surface of the palladium electrode (Volmer reaction)<sup>[29]</sup>.



A subsequent diffusion into subsurface layers leads to the formation of an absorbed palladium hydride species.



The desorption process is more complex, as not only the reverse of the mentioned reactions has to be considered. As further reactions Tafel (Eq.2.5) and Heyrovski (Eq.2.4) reactions can take place in hydrogen loaded palladium and lead to hydrogen evolution<sup>[29]</sup>.

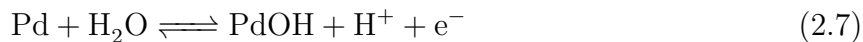
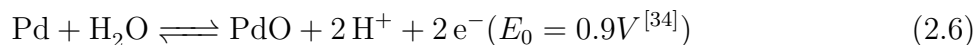


A direct absorption pathway has been proposed in literature<sup>[30-32]</sup> beside the reactions 2.2 and 2.3. According to these groups hydrogen can enter and escape the palladium metal without a prior adsorption step in this mechanism.

### 2.4.2 Palladium Oxide Formation

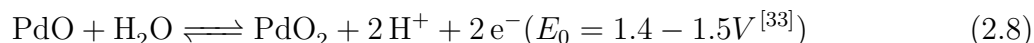
As palladium oxidation is basically a reaction of palladium with water, it appears in all aqueous electrolytes, which makes it the second important process in electrochemical experiments. PdO plays an important role in palladium dissolution<sup>[33]</sup>. Furthermore the electrochemical distinction of Pd(II)- and Pd(IV)-oxides (PdO and PdO<sub>2</sub>) allows a sophisticated method of surface area determination, which will be applied and discussed in Sec.4.6.

Two different oxidised species are proposed to form on palladium electrodes, PdO and PdOH.



The existence of the latter is not confirmed<sup>[33]</sup>, but for the sake of completeness it is given as additional possible reaction pathway. It should be noted that both mechanisms of oxide formation are dependent on the pH-value.

Further oxidation of PdO to higher valency oxides commences at higher potentials with the following underlying reaction:



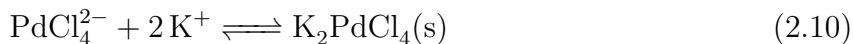
Oxidation of PdO is accompanied by oxygen evolution in this potential regime. For further reading on palladium oxidation and electrodisolution the review paper of Grdeń et al.<sup>[33]</sup> is suggested.

### 2.4.3 Formation of Palladium Complexes

In chloride ion containing solutions palladium readily forms soluble complexes. Besides, those can form insoluble precipitates in presence of suitable counter ions (cations). As an example for palladium-chloride-complexes the reaction to  $\text{PdCl}_4^{2-}$  can be written as



In potassium chloride solution,  $\text{K}_2\text{PdCl}_4$  is precipitated according to



It should be mentioned that other (e.g.  $\text{PdCl}_6^{4-}$ ) complexes, and precipitates, respectively, can form at higher potentials<sup>[35]</sup>, but they are of no additional importance for the experiments conducted within the scope of this thesis. From a chemical point of view palladium complex formation is an oxidation reaction - accordingly it results in a current peak on the anodic (upper) side in the voltammograms (compare Sec.4.7). Besides the aforementioned palladium oxide formation, this reactions (2.9 and 2.10) do also contribute to palladium dissolution.

# Chapter 3

## Experimental

### 3.1 Alloy Fabrication

Cobalt-Palladium master alloys in four different stoichiometries (A, B, C and D, see Tab.3.1) were prepared from Pd granules (AlfaAesar, 99.95%) and Co slug (AlfaAesar, 99.95%) via electron beam melting. The precursor material was weighed in the correct ratio (see Tab.3.1) to form approximately 1.5-2.0 g of each alloy. The electron beam melting was conducted at the Institute of Materials Science and Welding at the TU Graz. All compositions were melted multiple times at high beam currents to ensure complete mixing in the liquid state and consequently homogeneous single-phase alloys. The generated alloy drops were thinned to platelets (4-5mm in height) using a screw press. The further processing consisted of several consecutive rolling and annealing steps until a thickness of 250-270  $\mu\text{m}$  was reached. The annealing steps in a vacuum furnace (1 h, 700 °C,  $10^{-5}$  mbar) improved mechanical properties of the samples and were executed to avoid fracture in the rolling process. The resulting foil was cut into squares of 5x5 mm<sup>2</sup>, which were used as standard samples for the dealloying process. Homogeneity of all alloys was confirmed by XRD-measurements of the alloy platelets. One sample XRD spectrum for a CoPd80/20at% alloy can be found in figure 3.1. Clearly, the measured peaks lie in between theoretical peaks for palladium (at lower angles, blue) and cobalt crystals (at higher angles, red). As no marked peaks are visible at defined peak positions of palladium and cobalt, one can safely assume the formation of a homogeneous single-phase solid solution.

Table 3.1: Compositions and masses of the fabricated alloys

$C$  . . . . . composition  
 $m_{\text{Co}}$  . . . . . Weighed portion of Cobalt  
 $m_{\text{Pd}}$  . . . . . Weighed portion of Palladium  
 $m_{\text{tot}}$  . . . . . Total sample mass before melting

alloy	C / at%	C / wt%	$m_{\text{Co}}$ / g	$m_{\text{Pd}}$ / g	$m_{\text{tot}}$ / g
A	87.8-12.2	80-20	1.35	0.34	1.69
B	80-20	68.9-31.1	1.03	0.47	1.50
C	75-25	62.4-37.6	1.11	0.68	1.79
D	70-30	56.4-43.6	1.11	0.86	1.97

## 3.2 Electrochemistry

All Potentials measured in this thesis, unless stated otherwise, refer to the potential of the used Ag/AgCl (saturated KCl, Methrom) electrode. The standard electrode potential of this reference electrode is +0.197 V vs. SHE at room temperature (datasheet). Sulfuric acid was diluted from a 1M high purity standard solution (Roth 2N) with distilled water (Roth) to concentrations of 0.1M and 0.5M. KOH droplets (Roth  $\geq 85\%$  p.a.) and KCl salt were dissolved in distilled water to 1M potassium hydroxide solution and 1M potassium chloride solutions, respectively. 1M perchloric acid standard solution (Fluka Analytical 1N) was used in diluted (0.5M) form in the experiments.

### 3.2.1 Dealloying

The dealloying method and parameters in this work were adopted from Hakamada and Mabuchi<sup>[9]</sup>. They proposed an electrochemical etching process in 0.1 M  $\text{H}_2\text{SO}_4$  with a constant working electrode potential of +0.5 V vs. a saturated calomel electrode. This corresponds to +0.55 V vs. Ag/AgCl, which served as reference electrode in all measurements in this work. All dealloying experiments were performed until a residual current of 100  $\mu\text{A}$  was reached. This was intended to enable easier comparability of samples with different masses and compositions. Two different setups were used for dealloying in this work: free dealloying and in-situ dealloying in the dilatometer. Free dealloying must not be confused with free corrosion, the process of etching without applied potential, a technique which is not used in this work.

An Autolab PGSTAT128N potentiostat operated via the NOVA software was used to perform the free electrochemical measurements. For free dealloying the alloy samples (see Sec.3.1) were placed as working electrodes in a three-electrode electrochemical cell by carefully bend-

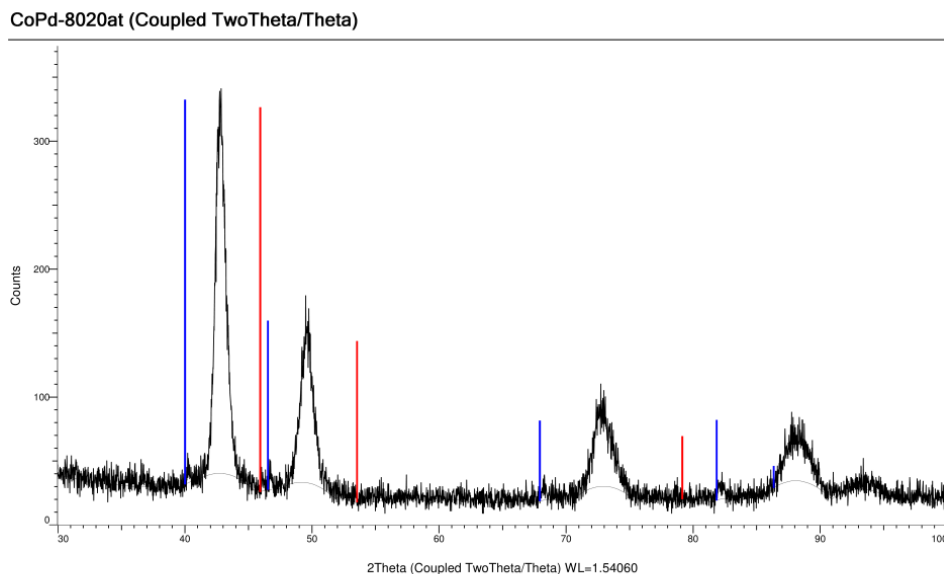


Figure 3.1: XRD spectrum of a CoPd80/20at% alloy platelet, red: reference peaks of Cobalt, blue: reference peaks of Palladium

ing a platinum wire around the platelets and connecting it to the potentiostat. Establishing a firm connection during the measurement, on the one hand, and allowing an easy removal of the brittle sample after electrochemical treatment, on the other hand, lead to this setup geometry. A coiled Pd-wire served as counter-electrode during dealloying. The setup for dilatometer dealloying as well as follow-up electrochemical treatments in the dilatometer will be described in the following section 3.2.2.

### 3.2.2 In-situ dilatometry

In this measurement setup an Autolab potentiostat (PGSTAT204) was used to control both voltage and current, while a Linseis L75 vertical dilatometer was used to track length changes simultaneously. The dilatometer, equipped with a hollow cylindrical quartz pushrod and a quartz sample holder, applied a constant force of 100 mN in all executed experiments, while measuring the pushrod displacement. The alloy samples were placed on a flattened platinum wire on the sample holder and fixed with the pushrod applying the selected constant force. A schematic drawing of the experimental setup is shown in Fig.3.2.

The dealloying process was executed analogously to the described process of free dealloying (Section 3.2.1). Since the geometry of the experiment leads to a reduced sample area exposed to the electrolyte this method is about 3 times slower than free dealloying of samples with a comparable mass. The electrochemical methods were conducted as described in section 3.2.3.

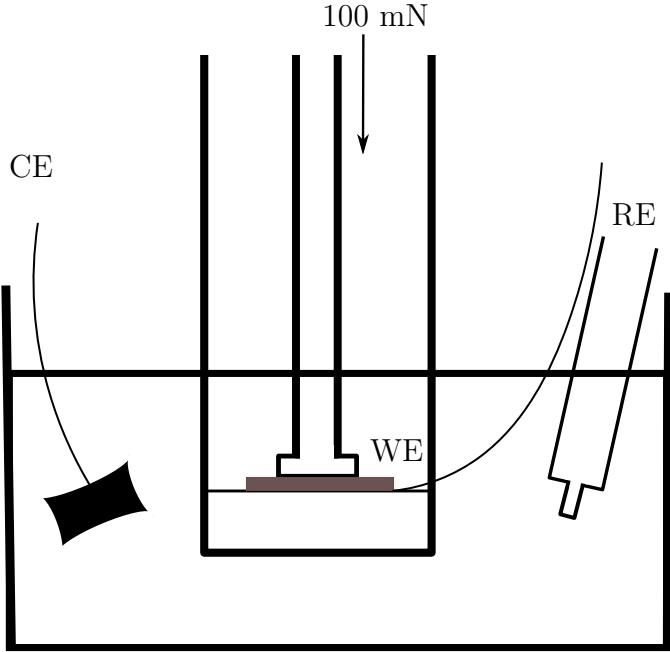


Figure 3.2: Experimental setup for in-situ dilatometry, schematic. The arrow indicates the force applied by the pushrod.  
WE.....working electrode  
CE..... counter electrode  
RE..... reference electrode

### 3.2.3 Electrochemical measurements after dealloying

After dealloying the measurement setup was immersed in distilled water to remove traces of the dealloying electrolyte from the nanoporous sample. After several hours in water, the sample was carefully dried with laboratory paper. The water was substituted with the electrolyte for the actual measurement, which is stated specifically for each sample in the results section. A highly porous carbon fabric connected via a platinum wire acted as counter electrode for nanoporous samples. In order to keep the current density at the counter electrode low, the surface of the counter electrode had to be chosen in this manner.

The first measurements after the dealloying process usually were CV measurements at low scan rates to investigate the primary oxide and to characterise the nanoporous samples. Due to the high surface area of the nanoporous samples the scan rate had to be small, as both surface area and scan rate are directly proportional to the current yield. For each measurement the scan rate ( $0.1 \text{ mVs}^{-1}$ ,  $0.5 \text{ mVs}^{-1}$  or  $1 \text{ mVs}^{-1}$ ) is stated explicitly in the results section. Chronoamperometric measurements were used to control hydrogen absorption in the nanoporous palladium samples. A list of all used samples for dilatometric measurements can be found in the following table (Tab.3.2).

Table 3.2: Sample labels and masses

The previously introduced abbreviations for initial compositions (A-80/20wt%, B-80/20at%, C-75/25at%, D-70/30at%) are used.

$m$  . . . . . Total mass of the initial alloy sample

$m_{\text{Co}-m}$  . . . . Cobalt mass calculated via the sample mass  $m$  and nominal alloy composition

$m_{\text{Pd}-m}$  . . . . Palladium mass calculated via the sample mass  $m$  and nominal alloy composition

Sample	$m / \text{g}$	$m_{\text{Co}-m} / \text{g}$	$m_{\text{Pd}-m} / \text{g}$
A1	0.068	0.0544	0.0136
A2	0.068	0.0544	0.0136
A3	0.067	0.0536	0.0134
A4	0.068	0.0544	0.0136
B1	0.072	0.0496	0.0224
B2	0.076	0.0524	0.0236
B3	0.066	0.0455	0.0205
B4	0.069	0.0475	0.0215
B5	0.065	0.0448	0.0202
B6	0.065	0.0448	0.0202
C1	0.078	0.0487	0.0293
C2	0.078	0.0487	0.0293
C3	0.073	0.0456	0.0274
C4	0.082	0.0512	0.0308
C5	0.062	0.0387	0.0233
D1	0.079	0.0446	0.0344
D2	0.082	0.0462	0.0358
D3	0.074	0.0417	0.0323
D4	0.082	0.0462	0.0358

# Chapter 4

## Results

### 4.1 Dealloying

In-situ dealloying in the dilatometer was conducted for 19 samples of different stoichiometries (see Tab.3.2) as described in Chapter 3. Current-time curves will be presented for selected samples in this section. During the dealloying process the dissolved cobalt ions turned the electrolyte pink, as described in the work of Hakamada and Mabuchi<sup>[9]</sup>. The length changes did not yield reproducible results, even for samples of the sample base alloy. The general dilatometric curves exhibited rather erratic strain behaviour with a total shrinkage of 20-40%.

The dealloying current per cobalt mass in the alloy sample is displayed in Fig.4.1 for four exemplary alloy samples of different composition. Within one stoichiometry the difference in sample mass alters the initial current and the shape of the dealloying curve to some extent, but the overall trend comparing different alloys remains unchanged. The dealloying process takes longer times at lower currents for samples containing lower amounts of the sacrificial element cobalt, whereas for alloys containing higher amounts of cobalt, currents are higher and the dealloying process is faster (see Sec.5.1). The generic shape of a dealloying curve in Fig.4.1 resembles an exponential decay up to a certain time when the current drops faster, but again almost exponentially.

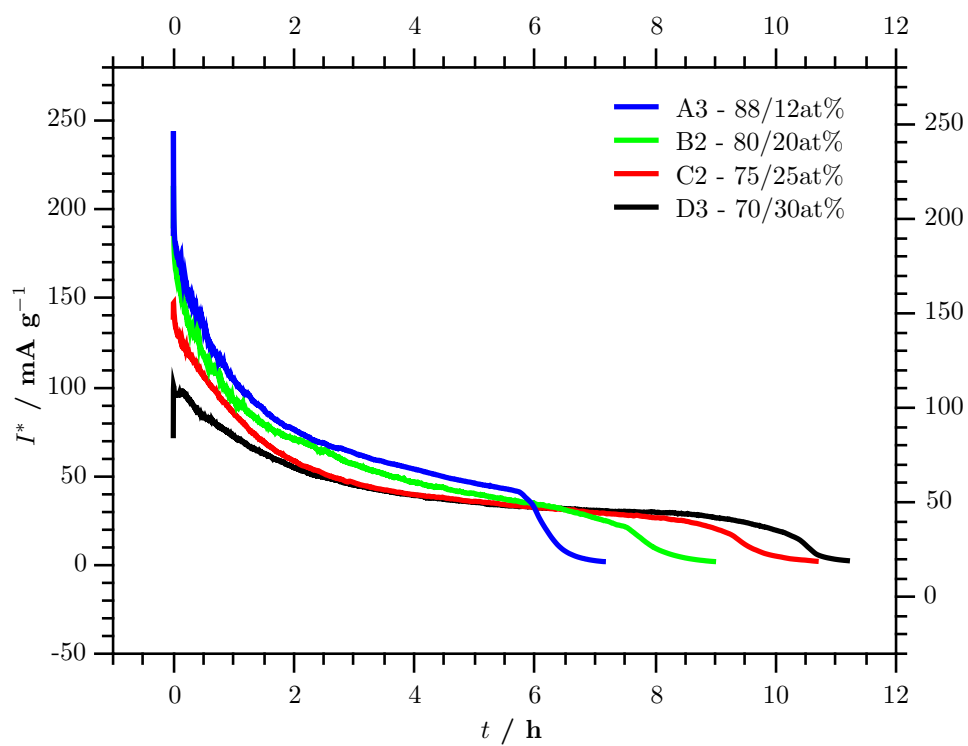


Figure 4.1: Current per cobalt mass  $I^*$  recorded as a function of time  $t$  during the dealloying process in 0.1 M  $\text{H}_2\text{SO}_4$  for different cobalt-palladium alloys: Samples of different stoichiometries (indicated by differently coloured curves) were held at a constant dealloying potential of  $U=0.55$  V (vs. Ag/AgCl).

## 4.2 CVs in Different Electrolytes

Cyclovoltammetric measurements were conducted for nanoporous Pd-samples prepared from alloy B (CoPd80/20at%) in  $\text{H}_2\text{SO}_4$ ,  $\text{HClO}_4$ , KCl and KOH solutions. In order to make measurements comparable the voltage window had to be adjusted according to the expected pH-values of the solutions, which can be calculated via the Nernst equation (Eq.2.1). The concentrations and the voltage ranges used in the experiments can be found in Tab.4.1. The scan rate was  $0.1 \text{ mVs}^{-1}$  in all 4 measurements.

Five cycles of each measurement are plotted in Fig.4.2. The general shape of the cyclic voltammogram in  $\text{H}_2\text{SO}_4$  (Fig.4.2 bottom left) has already been described in a previous section (see Fig.2.3). The voltammogram in KOH (Fig.4.2 top left) shows certain similarities to the one in  $\text{H}_2\text{SO}_4$ , but also exhibits specific features. The most obvious difference is the narrower double layer regime between -0.6 V and -0.5 V in the upper, anodic half cycle. The oxide region commences at -0.5 V and ranges up to the cathodic vertex potential of 0.4 V. The peak system in the hydrogen regime is located at voltages below -0.5 V on the lower, cathodic half-cycle and below -0.6 V on the upper half-cycle. The CV in potassium chloride solution (Fig.4.2 top right) shows a strong double peak between -0.45 V and -0.05 V on the cathodic side and a peak structure below -0.4 V on the anodic side, which distinguishes itself from the measurements in other electrolytes. The cause of this shape will be discussed later (Sec.4.7 and Sec.5.5). The cyclic voltammogram in  $\text{HClO}_4$  (Fig.4.2 bottom right) exhibits a large current peak in the hydrogen regime below 0 V. The remaining structural features in the oxide region therefore appear comparably small, their shape in fact is very similar to the oxide region in the CV in sulfuric acid to the left.

Table 4.1: Sample overview for the CVs in different aqueous electrolytes

sample	electrolyte	concentration	voltage range / mV	pH-value
B2	KCl	1 M	-800 to 350	7
B4	KOH	1 M	-1000 to 400	14
B5	$\text{H}_2\text{SO}_4$	0.5 M	-200 to 1200	0.3
B6	$\text{HClO}_4$	0.5 M	-200 to 1200	0.3

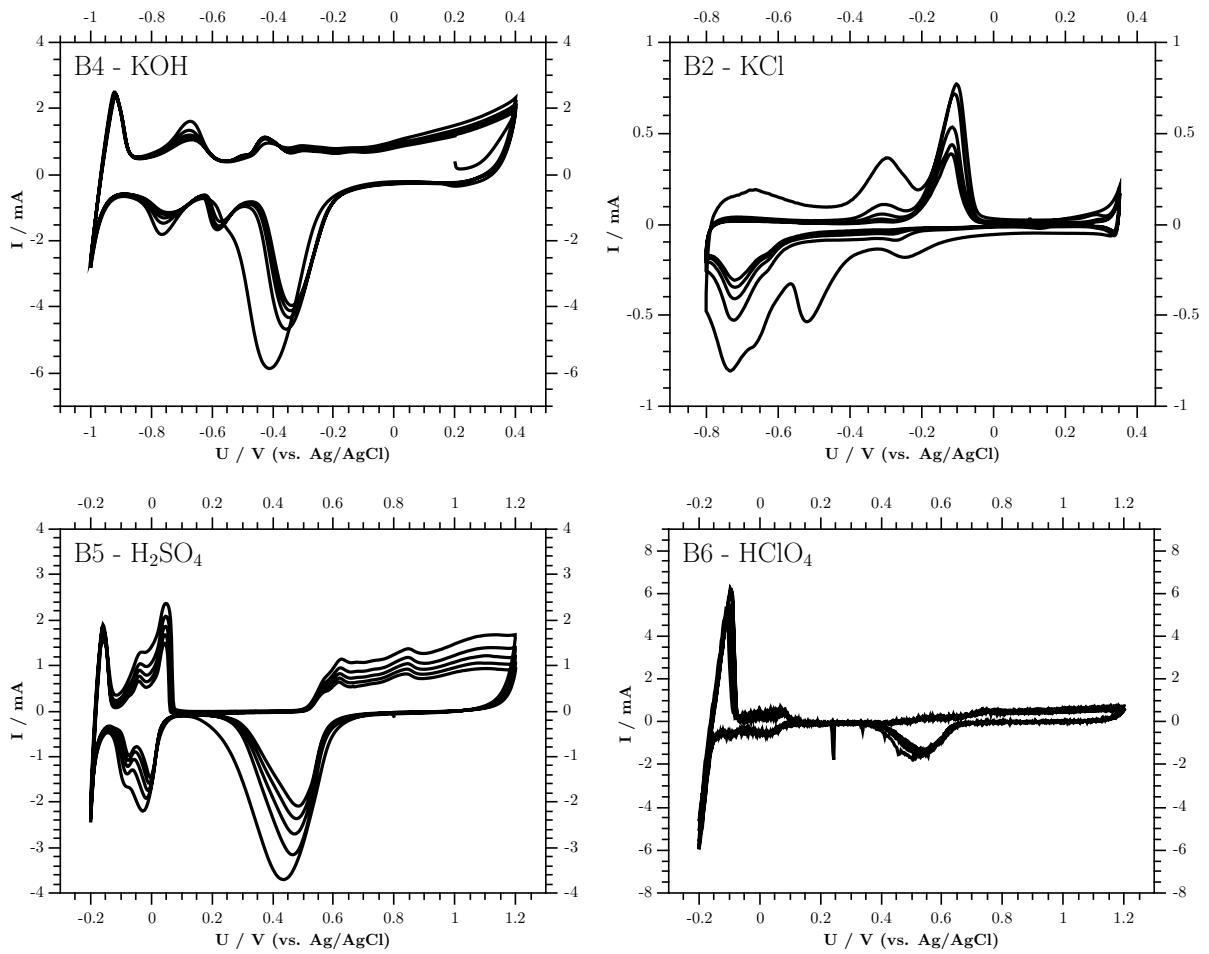


Figure 4.2: CV measurements of nanoporous palladium samples prepared from alloy B (CoPd80/20at%) in different electrolytes (1M KOH, 1M KCl, 0.5M H<sub>2</sub>SO<sub>4</sub> and 0.5M HClO<sub>4</sub> solutions) at a scan rate of 0.1 mVs<sup>-1</sup>, specific sample name is stated in the respective plot, 5 cycles are shown each, potential ranges were adjusted to the pH-value of the respective electrolyte to avoid gas evolution.

### 4.3 Hydrogen Storage in Nanoporous Palladium - Cyclic Voltammetric Studies

In order to investigate the influence of composition of the master alloy on the actual hydrogen storage properties of nanoporous samples, length changes were monitored during CV measurements in 1 M KOH. In a recent work of Steyskal et al. [2] the variations in length were measured for dealloyed nanoporous palladium from a CoPd alloy (CoPd80/20wt%) with the same setup as described in section 3.2.2 in 1 M KOH.

Samples from alloys A, B and C showed a reversible expansion at potentials below -0.6 V in the hydrogen region and a quasi-reversible expansion at potentials above -0.5 V in the oxide region. Strain-voltage and current-voltage curves for all initial stoichiometries at a scan rate of  $0.5 \text{ mVs}^{-1}$  are presented in Fig.4.3. The term quasi-reversible refers to the small strain offset after contraction in the oxide half-cycle, which will be discussed in a later section (5.5). The results presented in this section show similar tendencies in both hydrogen and oxide regimes with exception of a sample produced from alloy D (CoPd70/30at% - sample D1). The sample anomalously contracts in the region where hydrogen absorption is supposed to happen (see Fig.4.3). Further measurement on a different sample prepared out of alloy D confirmed this finding. This issue is addressed in detail in section 5.5.

Strains in all subsequent plots refer to the sample length after dealloying in the double layer regime. The total length changes in the hydrogen region at a scan rate of  $0.5 \text{ mVs}^{-1}$  vary from 0.4% for sample A1 to 0.75% for sample B4. The negative strain measured for sample D1 amounts -0.42%.

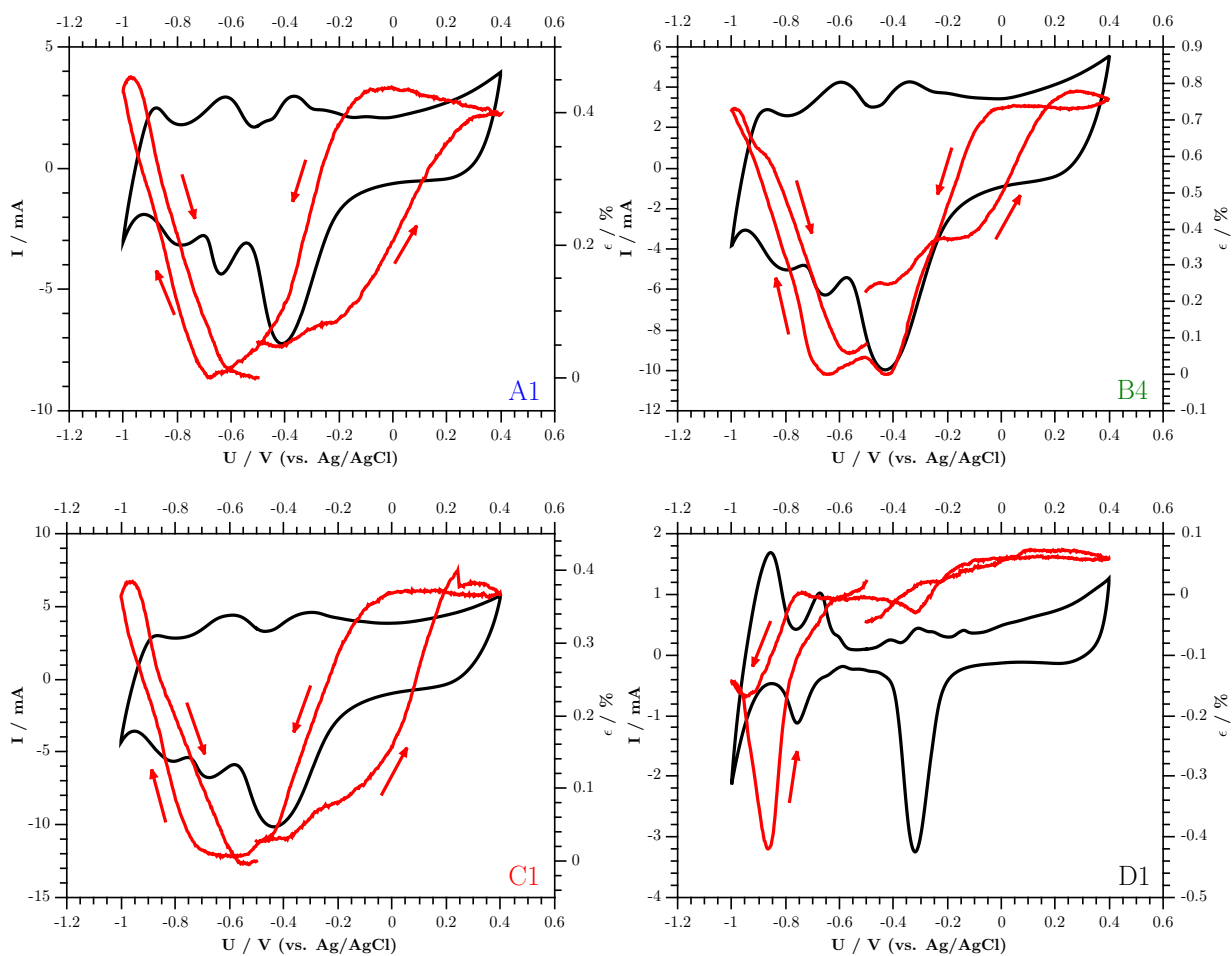


Figure 4.3: Length changes (red) and current (black) during a single voltammetric cycle in 1 M KOH for sample A1, B4, C1 and D1 (see inset). Zero on the strain axis was chosen at -0.5 V in the double layer regime, scan rate  $0.5 \text{ mVs}^{-1}$ .

## 4.4 Hydrogen Storage in Nanoporous Palladium - Chronoamperometric Studies

CA studies were performed for a more detailed characterisation in the hydrogen regime. Each loading experiment consisted of a CA loading step for 1h at selected potentials and was followed by an unloading step for 1h at -0.4 V, corresponding to a voltage in the double layer regime. The loading potentials in the hydrogen regime were chosen in intervals of 0.1 V starting from -0.6 V in KOH and decreasing from step to step. An additional measurement at -0.95 V was included for samples A, C and D. Integration of the resulting current-time curves during unloading enables the determination of the transferred charge and thus an estimation of the total hydrogen content ( $c_f$ -ratio, according to Eq.4.1) in the sample.

Due to weak Faradaic reactions at the electrode the current does not approach zero in practical experiments, but a steady value called leakage current instead. In order to correct the current for this contribution, an average current value for the last ten percent of the data points was subtracted from each individual value. Integration of the CA curves during loading instead of during the unloading process would yield too high currents and charges as a competing process of gaseous hydrogen evolution occurs at voltages below a critical potential.

The finally achieved atomic ratio of hydrogen and palladium  $c_f$  (H:Pd) was calculated according to

$$c_f = \frac{Q}{e \cdot N_A} \cdot \frac{M_{\text{Pd}}}{m_{\text{sample}}}, \quad (4.1)$$

where  $Q$  denotes the leakage-current-corrected integrated charge,  $M_{\text{Pd}}$  the molar mass of palladium (106.42 g/mol),  $m_{\text{sample}}$  the calculated net mass of the nanoporous sample after dealloying (no remaining cobalt assumed),  $N_A$  the Avogadro constant and  $e$  the elementary charge. The two latter constants are commonly combined to the Faraday constant.

Both  $c_f$  values and corresponding length changes allow a distinction between the two phases of palladium hydride. As discussed in section 5.5, these quantities also provide insight into mechanical properties of the palladium hydride system.

#### 4.4.1 Measurements in potassium hydroxide solution

A typical CA measurement of the unloading process in 1 M KOH at -0.4 V after previous polarisation at a potential of 0.95 V in the hydrogen regime is depicted in Fig.4.4. As stated above, integration over this curve gives the total amount of charge leaving the sample. Figure 4.5 shows the length changes corresponding to a series of loading-unloading procedures with decreasing loading potential in 1 M KOH for nanoporous palladium from all four initial stoichiometries plotted over time and hydrogen concentration. Loading processes are shaded grey in the plots, labelled with the corresponding polarisation potential. The unloading potential remained -0.4 V for all measurements and is therefore not stated explicitly in each plot. Individual CA measurements were recorded for one hour.

The last peak in each measurement run differs clearly from the preceding ones in both shape and height. During the last unloading process the sample contracts to a value smaller than the initial thickness, which is due to failing under the pressure of the dilatometer pushrod. As shown in Fig.4.5 The strain curve during the corresponding loading process at -1 V does not increase monotonously up to a plateau value, but rather shows an erratic increase in length until a maximum value is reached at the start of the subsequent unloading process. Causes for this behaviour are discussed in Sec.5.5.

An additional set of chronoamperometric loading experiments was conducted in 1 M KOH for samples of all stoichiometries using the free dealloying setup described in chapter 3. The aim of this measurement series was a detailed investigation of the palladium hydride phases present in the sample at different loading potentials, the corresponding diagram can be found in Fig.4.6(b). Furthermore the influence of the dilatometer can be estimated comparing both data sets.  $c_f$ -ratios are plotted over polarisation potential for all initial alloy compositions in Fig.4.6(b) for free dealloyed samples and in Fig.4.6(a) for samples dealloyed in the dilatometer setup. The potential in both plots refers to the reversible hydrogen electrode to enable comparison with literature data and with experiments in acidic electrolytes (see Sec.5.2).

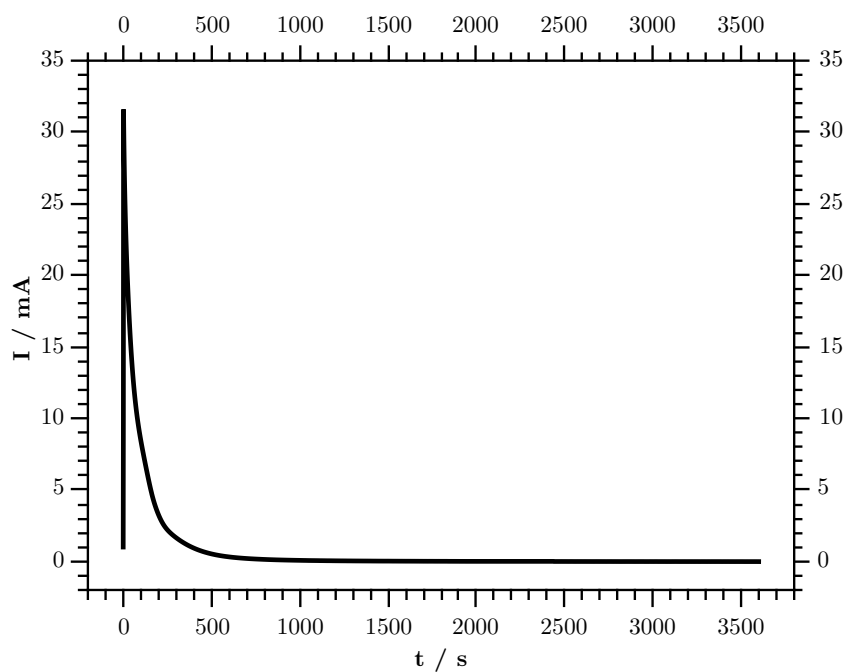


Figure 4.4: Current  $I$  as a function of time  $t$  for a characteristic unloading process in KOH at  $-0.4$  V after preceding polarisation at  $-0.95$  V (sample A1).

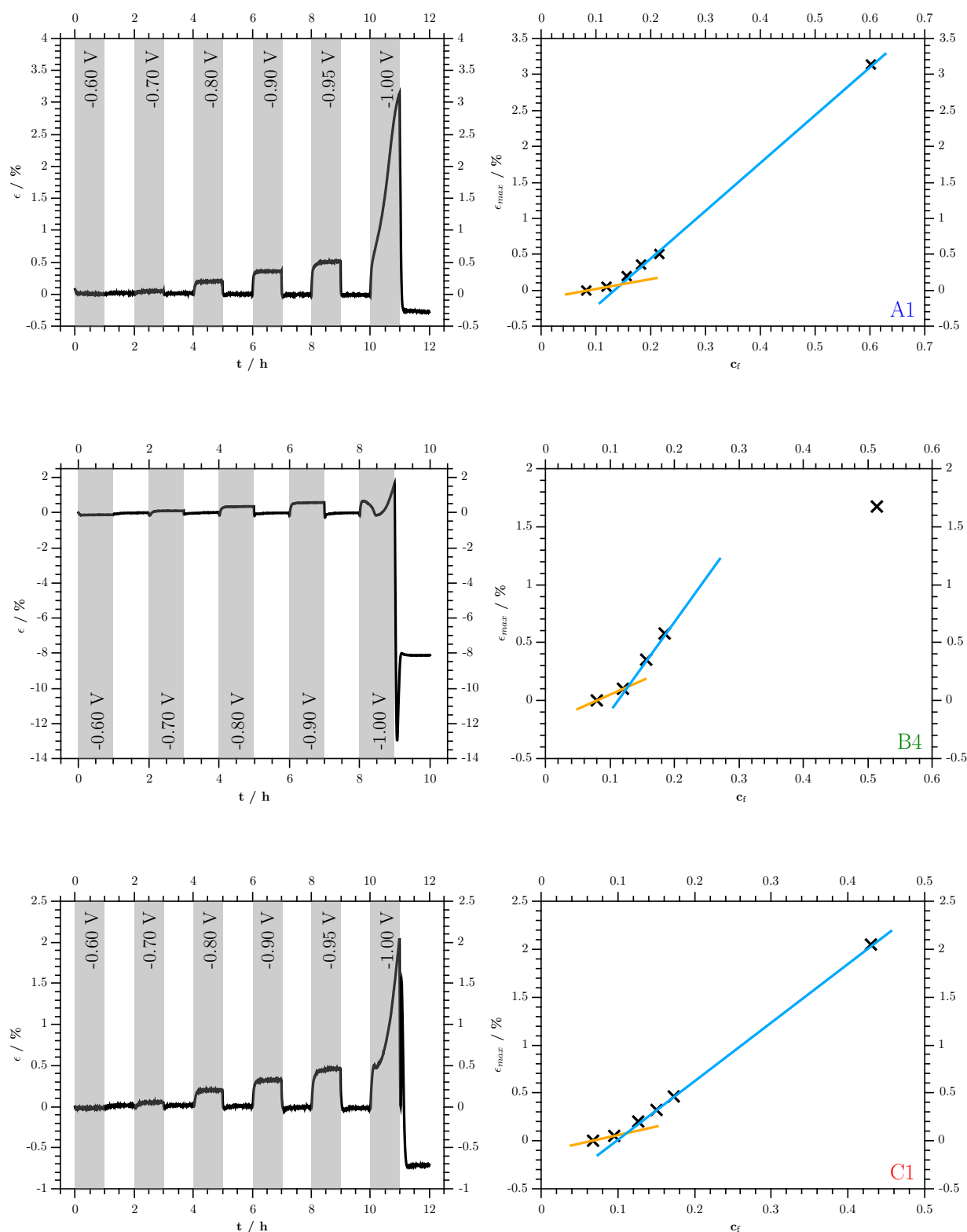


Figure 4.5: Hydrogen loading at constant potentials in 1 M KOH for samples A1, B4, C1 and D1 (see inset); left: elongation over time for a series of consecutive loading-unloading-processes, loading processes are shaded grey, polarisation potentials are given in the grey bars, the unloading potential remained -0.4 V; right: Maximum elongation over hydrogen concentration.

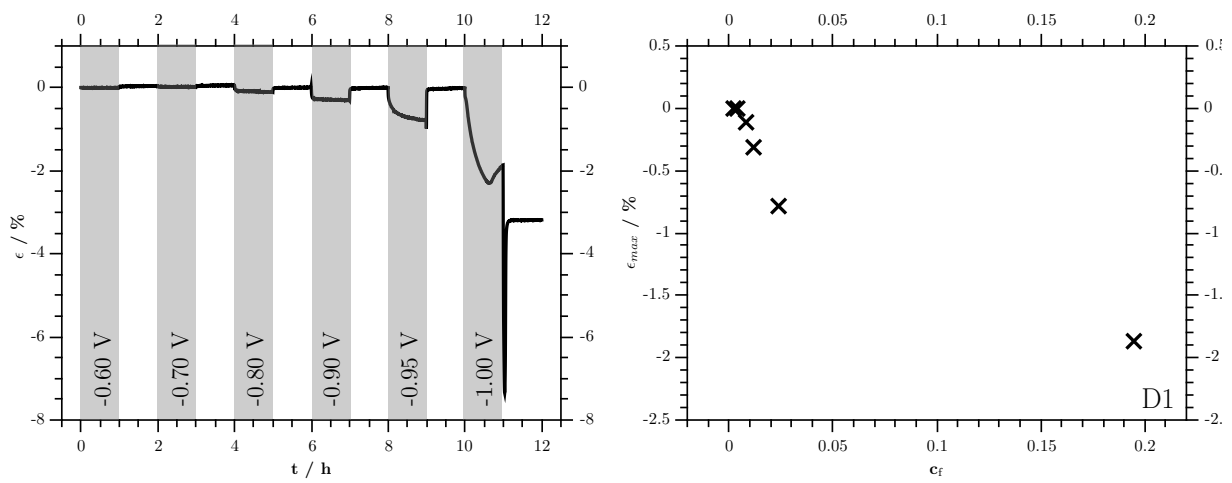


Figure 4.5: continuation from previous page

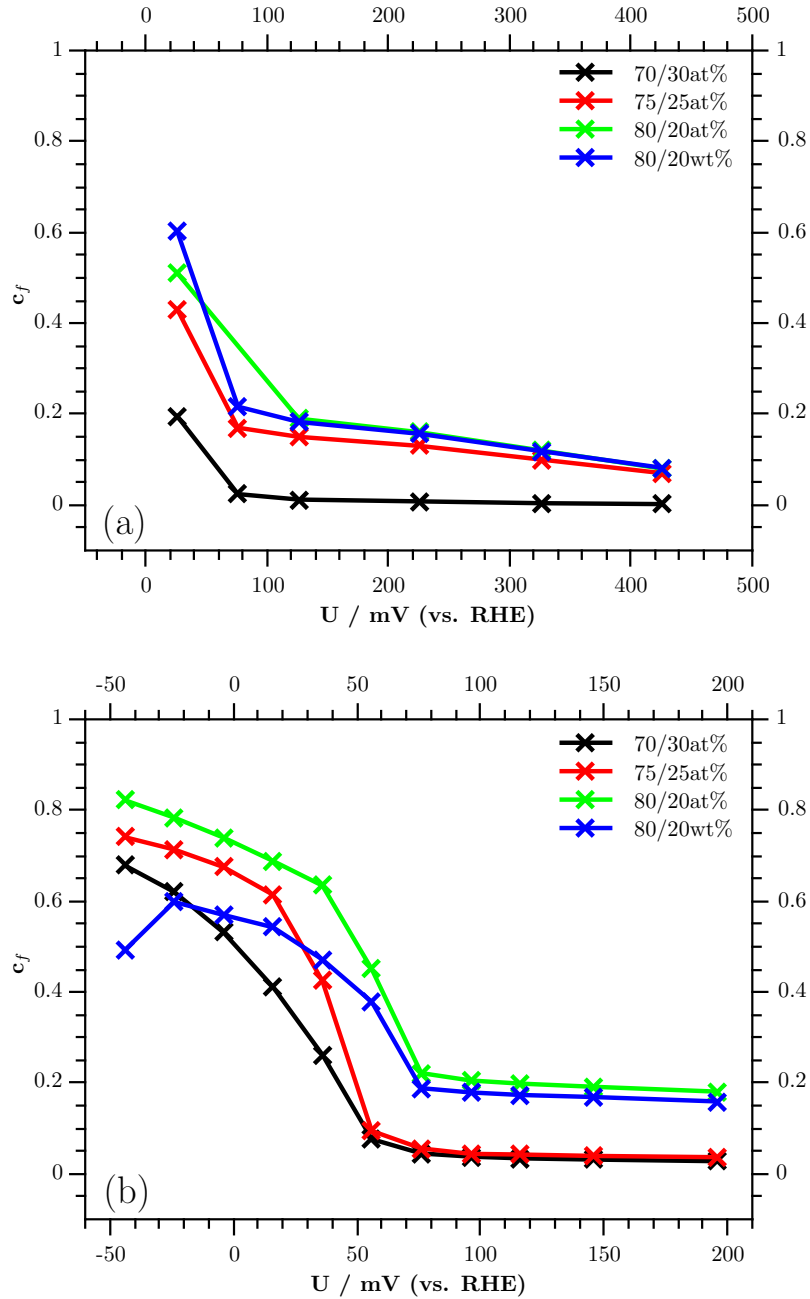


Figure 4.6: Atomic ratio of hydrogen and palladium  $c_f$  (H:Pd) as a function of polarisation potential  $U$  for samples in 1 M KOH (a) measured in the dilatometer setup and (b) measured with the free dealloying setup. Note the different voltage ranges on the x-axis in (a) and (b).

#### 4.4.2 Measurements in perchloric acid

Similar to the measurements described in the section above, nanoporous samples from alloys A, C and D were investigated regarding their loading behaviour in 0.5 M HClO<sub>4</sub> in the dilatometer setup. Once again, the atomic ratio of hydrogen and palladium  $c_f$  was plotted over polarisation potential (Fig.4.7).

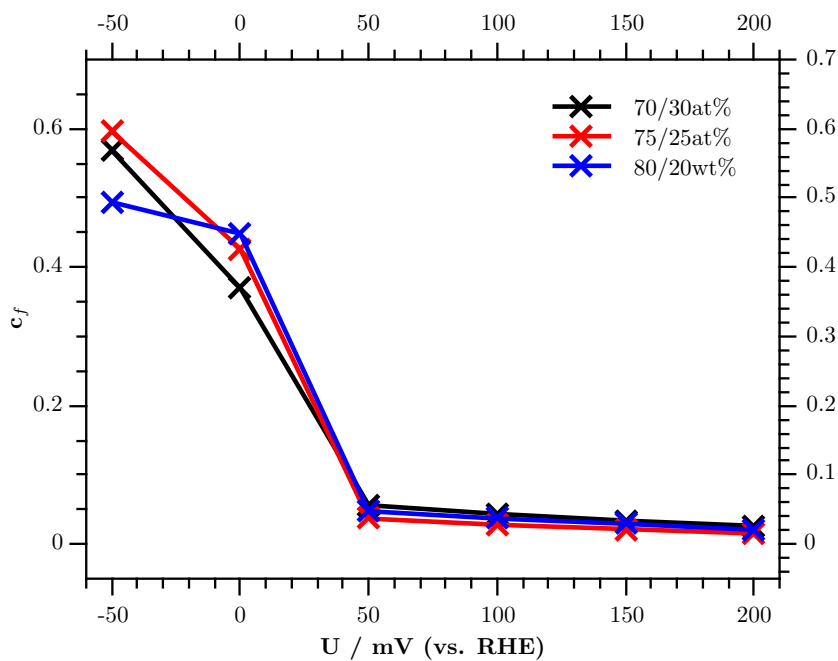


Figure 4.7: Atomic ratio of hydrogen and palladium  $c_f$  (H:Pd) as a function of polarisation potential  $U$  for samples measured in the dilatometer setup in 0.5 M HClO<sub>4</sub>.

## 4.5 Cyclic Voltammetry in the Hydrogen Regime

### 4.5.1 Nanoporous samples

Cyclovoltammetric experiments in the hydrogen regime (voltage range -1 to -0.5 V) at a scan rate of  $0.5 \text{ mVs}^{-1}$  were used to dynamically evaluate the strain-charge-behaviour of nanoporous palladium samples. Therefore CV currents were integrated numerically using the trapezoidal rule. Neither the shape of the CVs nor the strain response differed considerably from the corresponding part in the hydrogen regime of the full range CVs (Fig.4.3). The strain-charge-response in the hydrogen regime is illustrated in Fig.4.8 for nanoporous samples originating from all four initial stoichiometries.

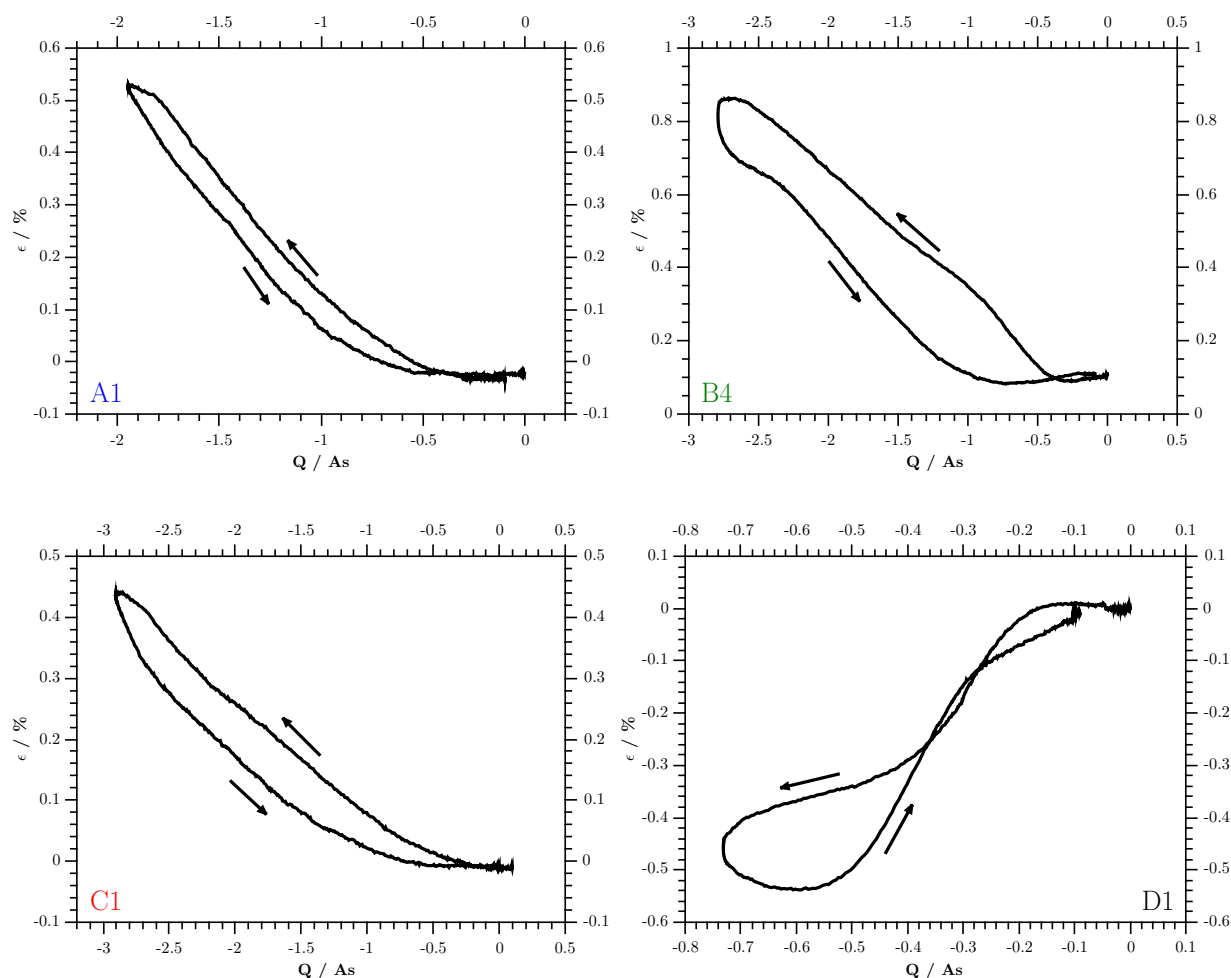


Figure 4.8: Length changes during a single voltammetric cycle in 1 M KOH for samples A1, B4, C1 and D1 (see inset) plotted over the corresponding charge, Zero on both strain and charge axis was chosen at  $-0.5 \text{ V}$ , scan rate  $0.5 \text{ mVs}^{-1}$ .

## 4.5.2 Palladium foil reference sample

For comparison a palladium sample cut from a Pd foil (Alfa Aesar, 0.25 mm, >99.98%) was placed as working electrode in the dilatometer setup. Measurements were conducted in 1 M potassium chloride solution at a scan rate of  $1 \text{ mVs}^{-1}$ . The current was corrected for a constant leakage current in the order of several  $\mu\text{A}$ . In Fig.4.9 the current during a CV measurement in the hydrogen regime and the corresponding strain are depicted. A strain-charge curve in analogy to the ones presented above for nanoporous samples can be found in Fig.4.9 on the right. The shape of the curve resembles the nanoporous samples, but the absolute values on both strain and charge axis are one order of magnitude lower in comparison with nanoporous palladium.

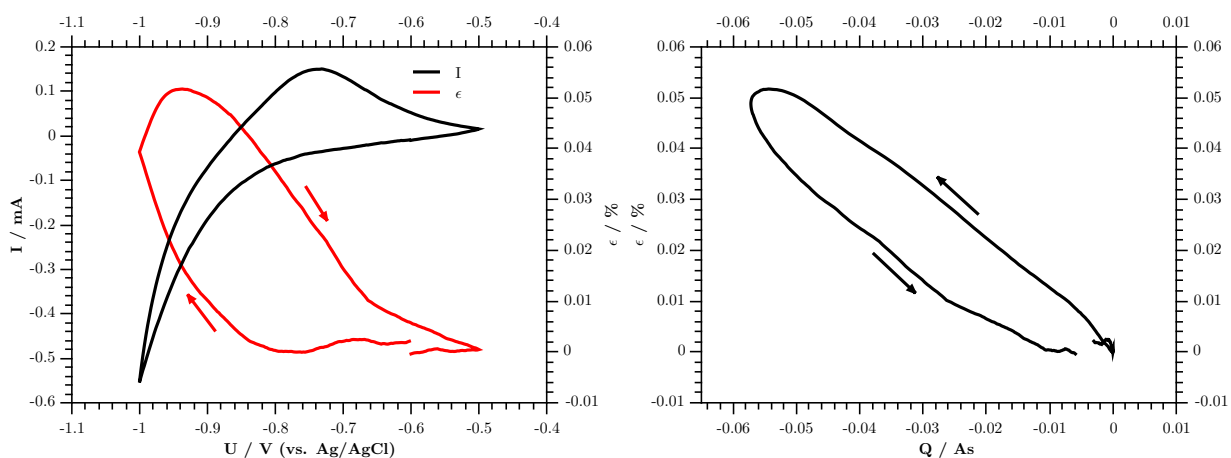


Figure 4.9: Length changes during a single voltammetric cycle in 1 M KOH for a Pd foil reference sample plotted over current (left) and the corresponding charge (right), Zero on both strain and charge axis was chosen at  $-0.5 \text{ V}$ , scan rate  $1 \text{ mVs}^{-1}$ .

## 4.6 Surface Area Determination

Two different electrochemical methods were applied to determine the specific surface area per unit mass of nanoporous palladium samples. Both methods were adopted from Fang et al. [36].

- Measuring the double layer capacitance via multiple CVs with different scan rates in the double layer regime
- Determining the charge for the formation of a palladium oxide monolayer via variation of the upper limit CV potential.

All measurements in this section were carried out in 0.5 M H<sub>2</sub>SO<sub>4</sub>. Plots of the CVs in the double layer region and the corresponding *I-s*-curves can be found in Fig.4.10. The slope of the regression lines (calculated) and values for the specific surface area are summarised in Tab.4.2.

For the set of CVs in the double layer regime scan rates of 0.1, 0.2, 0.5, 1, 2 and 5 mVs<sup>-1</sup> were used. For an ideal electrochemical double layer behaving as a capacitor the CV curves exhibit rectangular shape. On the one hand a deviation from the ideal shape is expected due to the ohmic resistance of the double layer, on the other hand it could indicate that Faradaic processes occur and the voltage range was not selected ideally, for comparison see Fig.4.10. A linear relationship between the scan rate *s* and the average plateau current in the centre of the double layer region *I*<sub>DL</sub> can be expected, with the capacitance *C*<sub>DL</sub> being the slope of that line:

$$C_{\text{DL}} = \frac{dQ}{dU} = \frac{I_{\text{DL}}dt}{dU} = \frac{I_{\text{DL}}}{s} \quad (4.2)$$

With a reference capacitance of 23.1 μF/cm<sup>2</sup> [36] for a smooth Pd electrode and the net palladium mass after dealloying the specific surface area (SSA) was calculated for samples of all initial stoichiometries using

$$A_{\text{DL}} = \frac{C_{\text{DL}}}{23.1\mu\text{F}/\text{cm}^2} \quad (4.3)$$

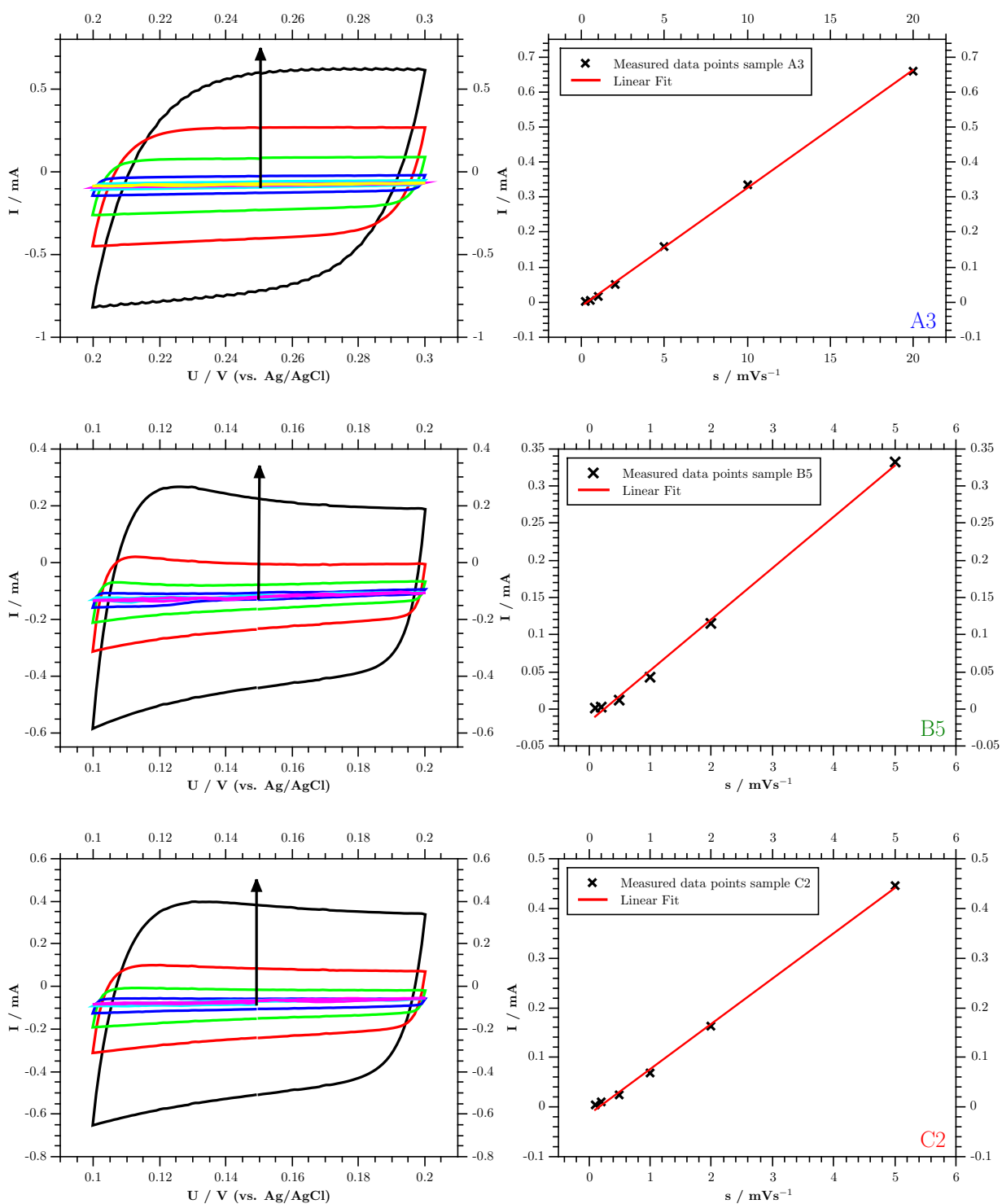


Figure 4.10: left: set of consecutive CV measurements in the double layer regime on samples A3, B5, C2 and D3 (see inset) in 0.5 M  $H_2SO_4$ . Scan rate: 0.1, 0.2, 0.5, 1, 2 and 5  $mVs^{-1}$  (arrow direction); right: plateau current versus scan rate.

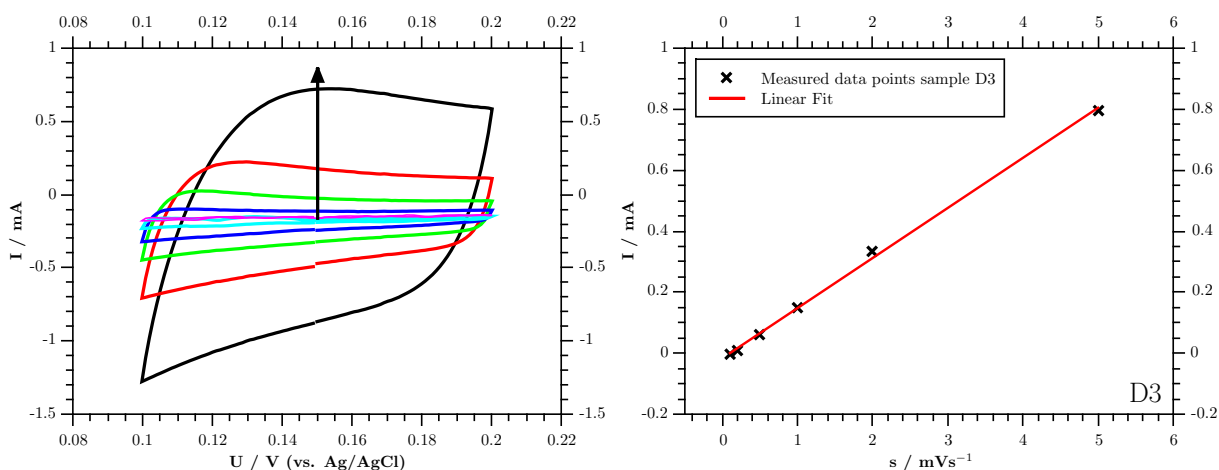


Figure 4.10: continuation from previous page

The second electrochemical method for surface area determination utilises the charge for the formation of a  $\text{Pd}^{2+}$  oxide monolayer. A reference charge per unit area can be calculated for adsorption on a Pd(100) plane and a charge transfer of 2 electrons per adsorbed atom to  $424 \mu\text{C}/\text{cm}^2$ <sup>[37]</sup>. The charge can be determined by varying the upper potential limit in the oxide region in a series of cyclic voltammograms with a scan rate of  $0.2 \text{ mVs}^{-1}$ . Numerical integration of the current associated with oxygen desorption corrected for the double layer current yields the corresponding charge to a maximum potential. The direct adsorption current cannot be used to determine the charge, as a concurrent process of oxygen evolution dominates the current at high potentials. Plotting charge over the maximum potential as in Fig.4.11, the curve behaves almost linearly with an inflection point at a certain voltage of about 1.2 V passing the curve into a region with a steeper slope.

The reason for the change in slope at 1.2 V is the onset of the formation of higher valency oxides, especially  $\text{Pd}^{4+}$  oxide, which start to grow after the first monolayer was formed<sup>[33,36–38]</sup>. Peaks attributed to the reduction of  $\text{Pd}^{2+}$  and  $\text{Pd}^{4+}$  oxides<sup>[33]</sup> can be identified in the CV measurements on nanoporous palladium samples (denoted A and B in Fig.4.11). In the above-cited paper by Grdeń et al.<sup>[33]</sup> a potential range of 1.4 to 1.5 V vs. RHE is given for the formation of the first monolayer Pd(II)O. This corresponds to the experiments in this work, for which the inflection point was found at potential values of 1.2 to 1.3 V vs. Ag/AgCl. The charge extrapolated from the  $Q$ - $U$ -diagrams at this point and the mass of the nanoporous palladium samples was used to calculate the specific surface area with this method. Cyclic voltammogram series for all samples and the corresponding  $Q$ - $U$ -curves can be found in Fig. 4.11. Charges associated with the formation of a PdO monolayer and the

resulting specific surface areas are summarised in Tab.4.2. For sample B5, originating from the CoPd80/20at% alloy, only a lower limit for the specific surface area could be extracted from the CV measurements, as the upper voltage limit was not chosen high enough to observe an inflection point in the  $Q$ - $U$ -curve (see Fig.4.11 - sample B5).

Table 4.2: Specific surface area of nanoporous palladium samples

$m_{\text{Pd}}$  ..... Mass of the nanoporous palladium sample (calculated, no residual cobalt assumed)  
 $k$  ..... Double layer capacitance of the samples as slope of the current vs. scan rate curves  
 $A_{\text{DL}}$  ..... Specific surface area determined via double layer capacitance  
 $Q$  ..... Charge associated with the formation of a PdO monolayer from Q-U-curves  
 $A_{\text{PdO}}$  ..... Specific surface area determined via charge for PdO monolayer formation

sample	composition	$m_{\text{Pd}}$ / mg	$k$ / F	$A_{\text{DL}}$ / $\text{m}^2\text{g}^{-1}$	$Q$ / C	$A_{\text{PdO}}$ / $\text{m}^2\text{g}^{-1}$
A3	80/20wt%	13.4	0.034	11.0	1.0	18
B5	80/20at%	20.2	0.069	14.8	> 1.1	> 13
C2	75/25at%	29.3	0.091	13.4	1.2	10
D3	70/30at%	32.2	0.164	22.0	2.3	17

Overall both methods are in good agreement, although they do not show the same trend for different alloys. Surface areas determined via double layer charging are largest for sample D (70/30at%) followed by sample B (80/20at%) with a significant margin and samples C (75/25at%) and A (80/20wt%). For the method utilising the oxidation charge of a PdO monolayer, alloy A exhibits the largest surface area with alloys D, B and C to follow. The value for alloy B lacks significance, as only a lower boundary was determined. The values are smaller than BET-measurements on nanoporous palladium samples produced via dealloying from PdAl alloys<sup>[39]</sup> ( $\sim 50$ - $70 \text{ m}^2\text{g}^{-1}$ ).

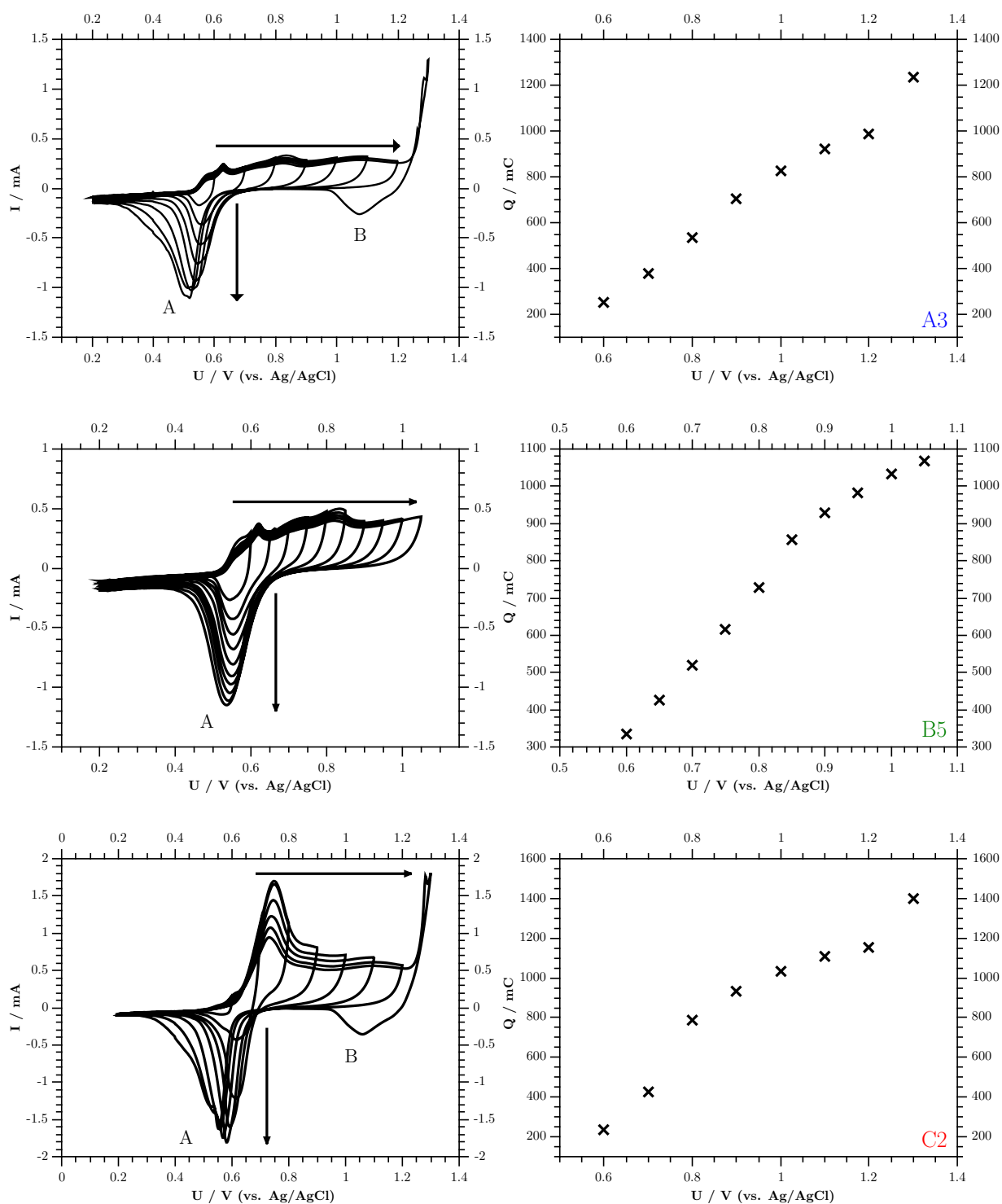


Figure 4.11: left: Subsequent CV measurements with increasing upper potential limits (arrow direction) for samples A3, B5, C2 and D3 (see inset). Scan rate:  $0.2 \text{ mVs}^{-1}$ ; right: charge versus maximum scan potential.

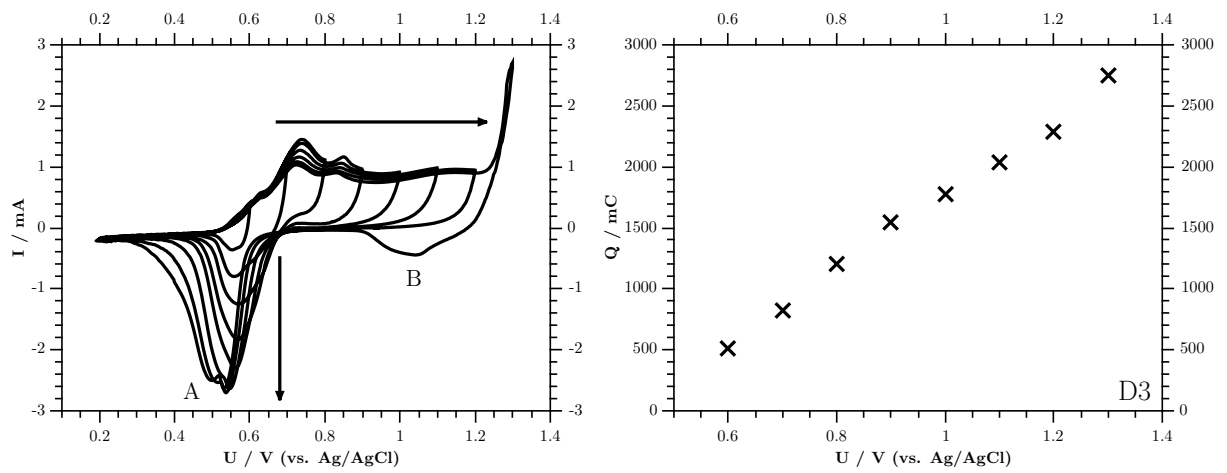


Figure 4.11: continuation from previous page

## 4.7 Length Changes in Acidic and Neutral Electrolytes

In this section length changes of nanoporous palladium samples during voltammetric cycling in different electrolytes ( $\text{H}_2\text{SO}_4$ ,  $\text{HClO}_4$  and  $\text{KCl}$  solutions) are examined. CV curves after the initial stripping process (the first voltammetric cycle) were recorded at a scan rate of  $0.1 \text{ mVs}^{-1}$  in the dilatometer for samples originating from alloy B (CoPd80/20at%). The measurement was conducted as described in the experimental section for in-situ dilatometry measurements. Strain/current over voltage curves are plotted in Fig.4.12.

For the experiment in 1 M potassium chloride solution a brown sediment was precipitated and the solution turned slightly yellow. The underlying reaction, which is also responsible for the large peak between -0.2 and 0 V in the CV (Fig.4.12-B5), is discussed later (Sec.5.5). In 0.5 M sulfuric acid a similar yellowish electrolyte discolouration was observed during the measurement, while precipitation did not take place in this case. The yellow colour could be attributed to  $\text{Cl}^-$ -ions in the solution probably due to a leak silver/silver chloride reference electrode, which uses a saturated  $\text{KCl}$  solution as internal electrolyte. The issue was resolved by using a silver/silver chloride reference electrode with a  $\text{KCl}/\text{KNO}_3$  salt bridge.

The irreversible decrease in length can be separated in contributions from different voltage ranges (roman numerals in Fig.4.12). Process I is present in acid and potassium chloride solutions in the hydrogen regime, e.g. at potentials  $<0.1 \text{ V}$  in acid and potentials  $<0.65$  in  $\text{KCl}$  solution. Contribution II is only present in  $\text{KCl}$  solution, where it occurs at potentials between  $-0.25 \text{ V}$  and  $-0.1 \text{ V}$ . Process III is again well-pronounced in acid and potassium chloride solution at potentials more positive than the double layer  $>0.5 \text{ V}$  in acidic solutions and at potentials  $>0 \text{ V}$  in  $\text{KCl}$  solution. The underlying mechanism responsible for the change in length is different for each region. Explanations for the different contributions are suggested in section 5.5. As CV measurements were conducted instantly after the initial stripping cycle, the cycle to cycle strain offset decreases with the number of cycles in all electrolytes. After sufficiently long times a constant actuation behaviour should ensue.

Irreversible length changes in  $\text{KOH}$  were weaker than in the other used electrolytes and become apparent only in terms of a small cycle-to-cycle offset in the strain curves in Fig.4.3. CV plots in potassium hydroxide solution were presented in a previous section (4.3).

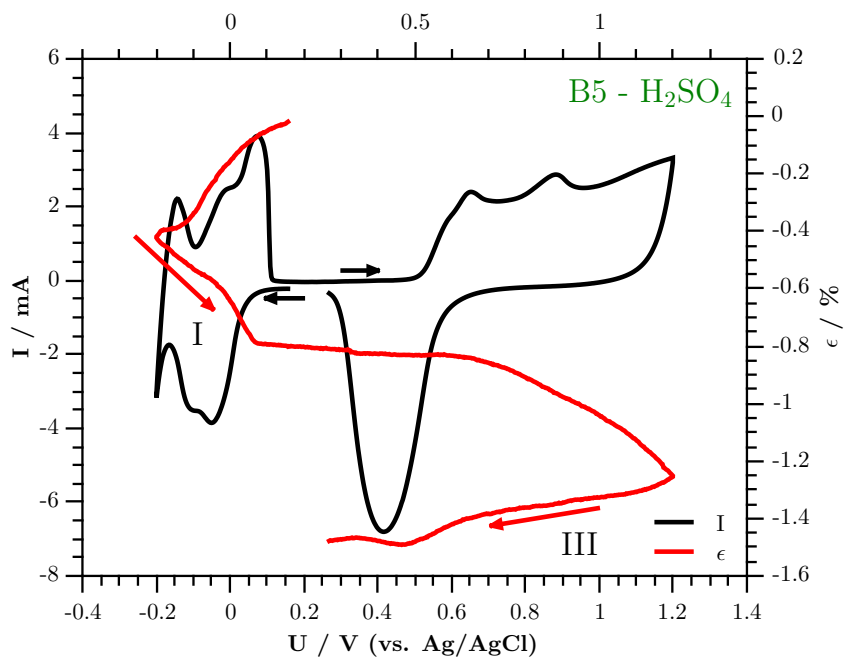
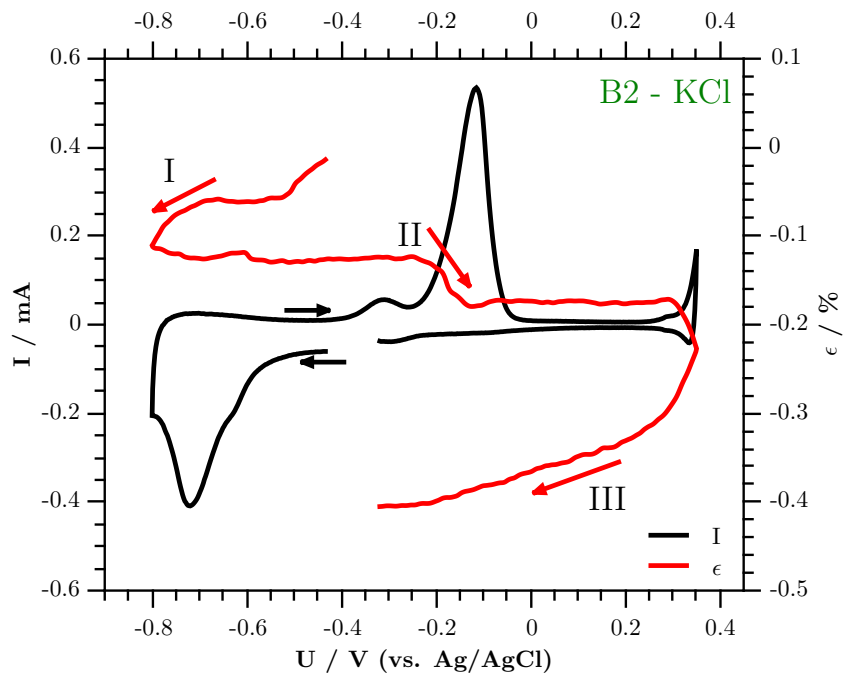


Figure 4.12: Length changes and current during a single voltammetric cycle on samples B2, B5 and B6 in 1 M KCl, 1 M H<sub>2</sub>SO<sub>4</sub> and 1 M HClO<sub>4</sub>, respectively (see inset). Zero on the strain axis was chosen arbitrarily.

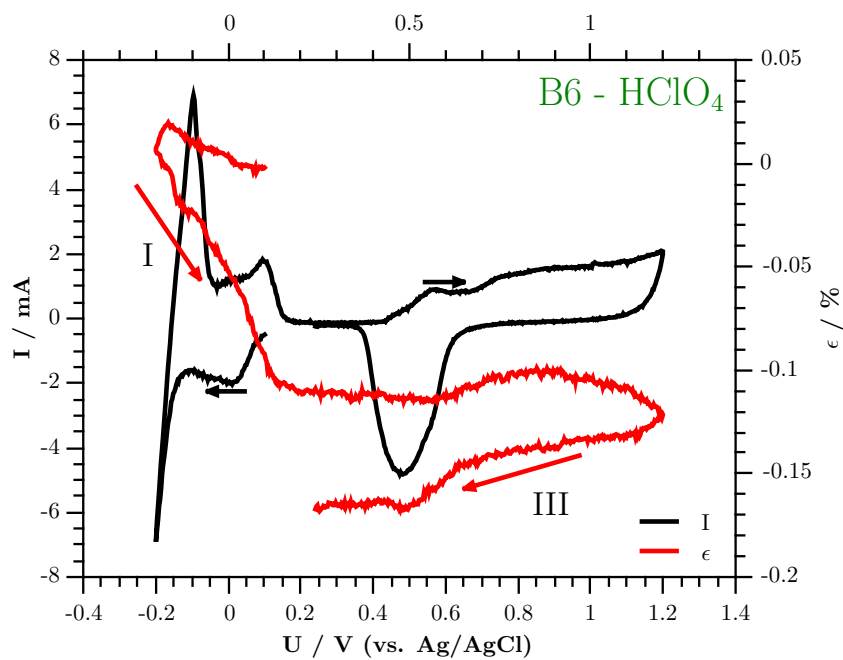


Figure 4.12: continuation from previous page

## 4.8 Scanning Electron Microscopy

For nanoscale materials scanning electron microscopy (SEM) is a powerful tool for structural characterisation. SEM measurements in this work were carried out at the Austrian Centre for Electron Microscopy and Nanoanalysis (FELMI-ZFE) with a FEI Quanta 600 and a Zeiss Ultra 55 microscope by Tobias Achtsnit and Sanja Simic. The original intention was a detailed imaging of the nanoporous structure at high resolution to evaluate the mean ligament size of the nanoporous structure for samples of all four initial compositions. As shown in a recent article<sup>[40]</sup> there is a simple relationship between the mean ligament width of a nanoporous palladium structure and its specific surface area, which makes scanning electron microscopy particularly attractive as a complementary method for surface area determination (compare Sec.4.6).

To avoid static charging effects on the sample surface, the as-dealloyed samples were reduced in 1 M KOH before investigation. Imaging with the FEI Quanta 600 microscope failed to produce satisfactory results, as the devices' resolution in general was too low for the nanoporous structure. With a Zeiss Ultra 55 microscope the pores could be resolved, but the imaging still turned out to be difficult, as the structure sizes also approached the resolution limit of this device. As a result, the obtained pictures were slightly blurred.

A selection of SEM images is presented in Fig.4.13-4.15. The available micrographs did not allow a quantitative analysis, but an overall impression of the nanoporous structure generated by the dealloying process could be gained. A comparison of structures evolving from different initial stoichiometries showed no clear trend regarding pore size.

Fig.4.13 shows the nanoporous structure of a sample from alloy B as dealloyed. Fine pores in the range of about 20nm are visible in the image.

Fig.4.14 shows a sample from alloy C, stripped in 1 M KOH. The estimated average pore size is in the range of 40 to 60nm, much larger than for the as-dealloyed sample. Furthermore, it could be argued that a hierarchical structure is present in Fig.4.14.

One set of samples was heat-treated in a vacuum furnace at 700°C and  $10^{-5}$  mbar for one hour (see Fig.4.15). It has previously been shown<sup>[9]</sup>, that such a heat treatment leads to a significant coarsening of the nanostructure, as the high surface to volume ratio is energetically unfavourable.

Images of nanoporous samples originating from alloy D (70/30at%) clearly revealed a modified surface morphology, appearing granular rather than porous (see for instance Fig.4.16). From SEM-investigations it is unclear if alloy D allows the formation of a nanoporous net-

work structure during the dealloying process.

Fig.4.15 shows a coarsened microstructure of a sample from alloy B, with ligament widths of about 200nm to 300nm and pore sizes of about half that size.

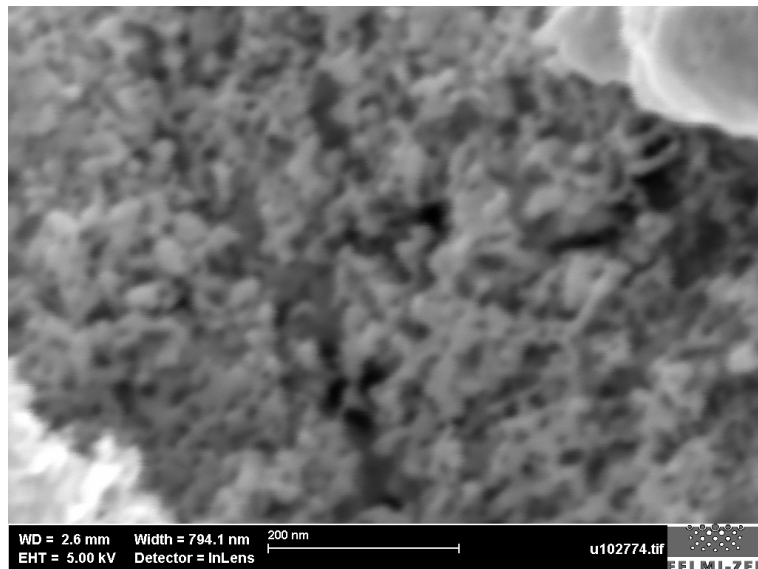


Figure 4.13: SEM micrograph of a nanoporous palladium sample originating from alloy B, as dealloyed. Image recorded with Zeiss Ultra 55 SEM.

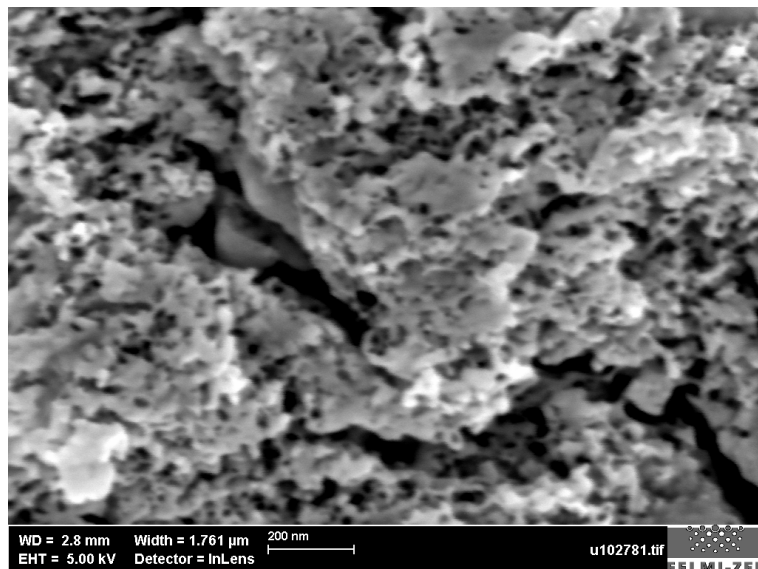


Figure 4.14: SEM micrograph of a nanoporous palladium sample originating from alloy C, stripped in 1 M KOH. Image recorded with Zeiss Ultra 55 SEM.

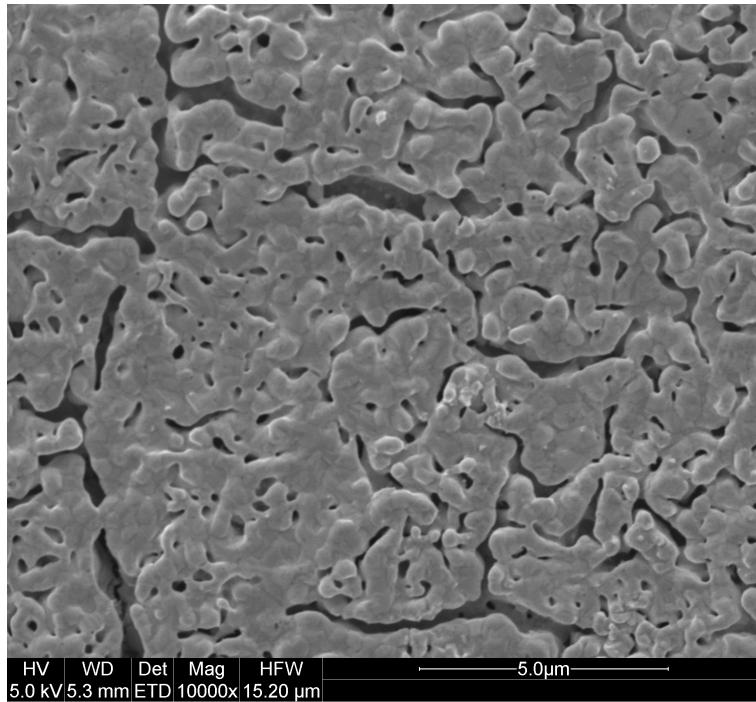


Figure 4.15: SEM micrograph of a nanoporous palladium sample originating from alloy B, coarsened at 700°C for 1 h. Image recorded with FEI Quanta 600.

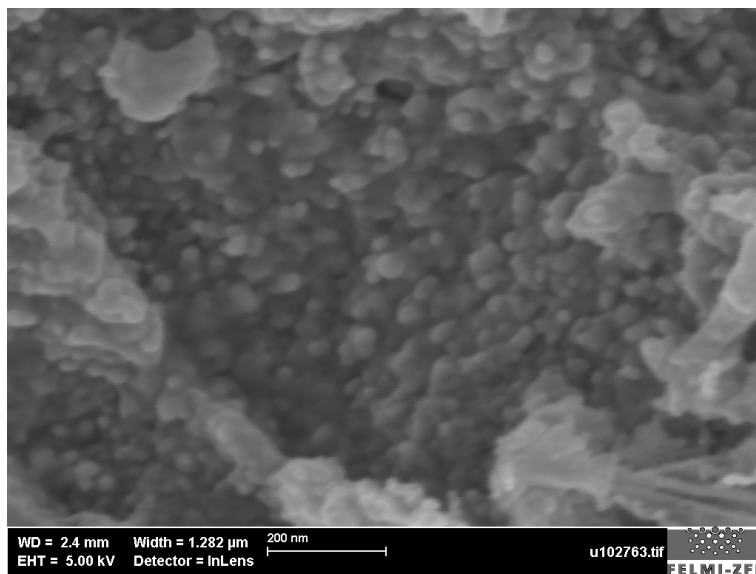


Figure 4.16: SEM micrograph of a nanoporous palladium sample originating from alloy D, stripped in 1 M KOH. Image recorded with Zeiss Ultra 55 SEM.

# Chapter 5

## Discussion

### 5.1 The Dealloying Process

Comparing the different dealloying curves in Fig.4.1, it can be seen that the dealloying time decreases with increasing cobalt concentration in the alloy. At first glance, this behaviour might seem counter-intuitive. However, it can be explained using the dealloying model suggested by Erlebacher et al.<sup>[41]</sup>: The model essentially describes the dealloying process as a two-step mechanism, consisting of dissolution of the sacrificial element and diffusion of the more noble element at the sample-electrolyte interface. As the dealloying process was faster for samples with higher cobalt contents in this work, cobalt dissolution must be a fast process compared to palladium surface diffusion. One can draw the conclusion that surface diffusion of palladium atoms must clearly be the rate-limiting process regarding dealloying kinetics of palladium-cobalt-alloys. For the sake of completeness it should be mentioned that the dealloying process in general is limited by surface diffusion, as electrolyte diffusion of dissolved atoms proceeds nearly 10 orders of magnitude faster<sup>[42]</sup>.

In order to estimate the content of residual cobalt in the nanoporous samples, the charge quantity involved in the dealloying process was determined via trapezoidal integration of the current curves (e.g. Fig.4.1). Assuming no additional electrochemical processes, the mass of dissolved cobalt,  $m_{\text{Co-Q}}$ , can be calculated as

$$m_{\text{Co-Q}} = \frac{Q \cdot M_{\text{Co}}}{2 \cdot e \cdot N_{\text{A}}} \quad (5.1)$$

with  $Q$  the dealloying charge,  $M_{\text{Co}}$  the molar mass of cobalt,  $e$  and  $N_{\text{A}}$  the usual physical constants. The factor of 2 has to be added for the 2+ -ionisation of Co-ions.

Table 5.1: Dealloying process characteristics for samples from all initial alloy stoichiometries, the previously introduced abbreviations for initial compositions (A-80/20wt%, B-80/20a%, C-75/25a%, D-70/30a%) are used.

$Q$ ..... Charge quantity involved in the dealloying process  
 $m$ ..... Total mass of the initial alloy sample  
 $Q/m$ ..... Specific charge per unit mass of the initial alloy  
 $m_{\text{Co}-m}$ .... Cobalt mass calculated via the sample mass  $m$  and the nominal alloy composition  
 $m_{\text{Co}-Q}$ .... Cobalt mass calculated via total charge  $Q$  according to Eq.5.1  
 $\eta$ ..... Dealloying efficiency as ratio of cobalt masses calculated from charge and mass

Sample	Q / As	m / g	Q/m / As/g	$m_{\text{Co}-m}$ / g	$m_{\text{Co}-Q}$ / g	$\eta$
A1	177.0	0.068	2603	0.0544	0.0541	0.994
A2	170.4	0.068	2505	0.0544	0.052	0.956
A3	175.6	0.067	2621	0.0536	0.0536	1
A4	173.0	0.068	2545	0.0544	0.0528	0.971
B1	159.8	0.072	2220	0.0496	0.0488	0.984
B2	171.3	0.076	2254	0.0524	0.0523	0.998
B3	146.6	0.066	2222	0.0455	0.0448	0.984
B4	155.3	0.069	2251	0.0475	0.0474	0.998
B5	152.7	0.065	2349	0.0448	0.0466	1.040
B6	143.9	0.065	2213	0.0448	0.0439	0.981
C1	157.0	0.078	2013	0.0487	0.0479	0.984
C2	154.8	0.078	1984	0.0487	0.0473	0.971
C3	147.8	0.073	2024	0.0456	0.0451	0.990
C4	162.9	0.082	1986	0.0512	0.0497	0.971
C5	124.9	0.062	2014	0.0387	0.0381	0.985
D1	143.3	0.079	1814	0.0446	0.0438	0.981
D2	149.0	0.082	1817	0.0462	0.0455	0.985
D3	130.7	0.074	1766	0.0417	0.0399	0.957
D4	149.2	0.082	1820	0.0462	0.0456	0.986

The calculated values for the cobalt masses, specific charge and dealloying efficiency are listed in Tab.5.1 for samples from all initial compositions. The nominal cobalt content of the alloy sample can be calculated using the sample mass and the mass concentration of the respective alloy, which can be found in Tab.3.1. The specific charge per unit mass  $Q/m$  of the initial alloy is also calculated, which is approximately constant for one composition. The value  $\eta$  represents the mass ratio of dissolved cobalt atoms (calculated via charge) and the total number of cobalt atoms (calculated via nominal composition), which should be 1 for an ideal dealloying process leaving no residual cobalt in the nanoporous structure. Thus,  $\eta$  can be considered as a measure for the efficiency of the dealloying process. The efficiencies for the dealloying process, as listed in Tab.5.1, are well above 95%, regardless of the initial composition.

A secondary electrochemical process is the aforementioned oxide formation on the sample surface during dealloying. In voltammetric measurements the first cycle exhibits an extraordinarily large oxygen desorption peak, which is shifted to lower voltages, indicating the presence of a strongly bound oxidised species. In the present study this effect was measured, although the magnitude of the first desorption peak is small compared to the measurements on platinum in the work of Steyskal et al.<sup>[17]</sup>. Integrating over the first and the subsequent desorption peak yields a charge difference of less than 2 As for all nanoporous palladium samples, directly stripped after dealloying. Therefore the above-calculated efficiency  $\eta$ , neglecting oxide formation, can only give an upper boundary, however, based on the primary oxide desorption peak, the contribution of oxidation can reasonably be considered small.

Another factor which might alter the efficiency values in Tab.5.1 is the homogeneity of the alloy samples. As previously mentioned (Sec.3.1), XRD-measurements confirmed the homogeneity of the thick CoPd-samples, but as this method is particularly surface sensitive, there might have been single phase cobalt or palladium grains inside the sample, which could alter the local composition after the rolling process. With the results from Tab.5.1 and the above mentioned uncertainties it can still reasonably be assumed that the dealloying process results in very low residual cobalt concentrations, which is in good agreement with literature where a dissolution more than 98% of the initially present cobalt was reported for dealloying with similar parameters<sup>[27]</sup>.

## 5.2 Potential Dependence of Hydrogen Concentrations - Palladium Hydride Phases

It is well known in literature that a distinction of palladium hydride phases is possible by plotting the hydrogen concentration as a function of potential<sup>[29,31,32]</sup>. Following these references, such plots were created by performing a series of loading and unloading experiments with a changing polarisation potential, as described in section 4.4. The respecting plots can be found in Fig.4.6 for experiments in KOH solution. At high potentials the atomic ratio of hydrogen and palladium was found to be close to zero for the samples dealloyed from alloy D (70/30at%). The freely dealloyed sample from alloy C shares this behaviour. The other nanoporous samples from alloys A,B and C show  $c_f$ -ratios higher than 0.15 at 200mV. This  $c_f$ -ratio or hydrogen concentration, respectively, can mainly be attributed to hydrogen adsorption onto the surface of nanoporous samples according to the reaction 2.2 described in section 2.4. The high concentration of about 0.15 can be explained by the high surface-to-volume ratio of the nanoporous samples. The absence of this enhanced  $c_f$ -ratio in samples from alloy D and a freely dealloyed sample from alloy C could be an indicator for an altered surface structure of those samples. In the case of alloy D a modified surface morphology is supported by the SEM micrographs in Sec.4.8 (Fig.4.16).

The onset of  $\beta$ -phase formation was found at around 70mV (see Fig.4.6) for all samples regardless their initial composition. According to Singh et al.<sup>[29]</sup> the coexisting  $\alpha$ - and  $\beta$ -phases ranges from a  $c_f$ -ratio of 0.06 to a  $c_f$ -ratio of 0.38. The  $\beta$ -phase saturates at different potentials for samples from different master alloys, showing a trend shifting to lower potentials for higher initial palladium contents in the alloy (alloy A  $\sim$  55mV, B  $\sim$  35mV, C  $\sim$  15mV, D  $<$  0mV). Down to this voltage  $\alpha$ - and  $\beta$ -phase coexist. It is apparent that for the sample with the lowest initial palladium content in Fig.4.6(b) (blue curve) lower hydrogen concentrations were reached compared to Fig.4.6(a). In Fig.4.7 the  $c_f$ -ratios were plotted over polarisation potential for experiments in HClO<sub>4</sub>. Due to the reduced number of measurement points a clear definition of an onset potential of  $\beta$ -phase formation is difficult, but a value of  $\sim$ 70 mV(vs.RHE) seems plausible. The same problem is still present for the potential of  $\beta$ -phase saturation, but the trend of lower values for higher initial palladium contents could hold for measurements in HClO<sub>4</sub> again.

### 5.3 Quantitative Evaluation of Actuation

Potentiostatic charging experiments of samples from all initial stoichiometries in 1M KOH solution were presented in section 4.4. Resulting plots of atomic ratio of hydrogen and palladium H:Pd ( $c_f$ ) and maximum elongation ( $\epsilon_{\max}$ ) can be found in Fig.4.5. Due to the anomalous behaviour of samples from alloy D (CoPd70/30at%) a separate section is dedicated to their discussion (Sec.5.4). Although the number of data points is limited in all graphs, two different slopes (or strain coefficients  $\frac{\Delta\epsilon_{\max}}{\Delta c_f}$ ) can be clearly identified, which are plotted as straight lines in the graphs. A smaller slope up to a  $c_f$ -ratio of about 0.15 was fitted linearly for the first two data points (orange line) and an increased slope at higher  $c_f$ -values was fitted linearly for the remaining data points (blue line). The last data point in Fig.4.5-B4 was excluded from the linear fit, as the sample yields already during the loading procedure and the attained maximum strain of 1.7% can be assumed to be too low.

This dual slope linear fit represents a more detailed description of the hydrogenation process in this material, which was previously investigated and described by a simplified single-slope approximation by Steyskal et al. [2]. However also the data points presented in their work suggest, that a precise description of hydrogen-charging requires a dual-slope linear fit as proposed in the present work.

Electrocapillary coupling coefficients, which are commonly used in literature to quantify electrochemical actuation<sup>[4,43]</sup>, were calculated using the following equation<sup>[4]</sup>:

$$\zeta = -\frac{9Km_{\text{sample}}}{2\rho} \cdot \frac{\Delta\epsilon}{\Delta Q} \quad (5.2)$$

where  $\zeta$  denotes the electrocapillary coupling coefficient,  $K$  the bulk modulus of palladium (180 GPa<sup>[4]</sup>),  $m_{\text{sample}}$  the sample mass,  $\rho$  the palladium density (12023 kgm<sup>-3</sup><sup>[4]</sup>),  $\Delta\epsilon$  the macroscopic strain and  $\Delta Q$  the transferred charge.

Both strain coefficient ( $\frac{\Delta\epsilon_{\max}}{\Delta c_f}$ ) and electrocapillary coupling coefficient ( $\zeta$ ) are measures for the attainable elongation corresponding to a fixed amount of charge. Values can be found in Tab.5.2. As the strain energy density of actuator materials scales with the squares of maximum elongation<sup>[4]</sup>, values for the maximum elongation<sup>[4]</sup> are also listed in the table below (Tab.5.2).

Using the relation between  $Q$  and  $c_f$  (Eq.4.1) one can express  $\zeta$  as:

$$\begin{aligned}\zeta &= \frac{9KM_{\text{Pd}}}{2eN_A\rho} \cdot \frac{\Delta\epsilon_{\text{max}}}{\Delta c_f} \\ &= 0.741\text{V} \cdot \frac{\Delta\epsilon_{\text{max}}}{\Delta c_f}\end{aligned}\tag{5.3}$$

As a larger negative charge corresponds to a higher  $c_f$ -ratio, a negative sign had to be added in Eq.4.1.

The largest elongation during potentiostatic charging in the hydrogen regime of 3.1 % relative to the double layer regime at a  $c_f$ -ratio of 0.6 was obtained for a nanoporous sample from alloy A (80/20wt% - compare Fig.4.5). Nanoporous palladium prepared by dealloying from the same stoichiometry was reported to exhibit a reversible strain of more than 5 % during both potentiostatic and galvanostatic charging in 1M KOH solution<sup>[2]</sup>, which is the highest reversible strain for nanoporous metals to date. Although this record could not be equalled in the present work, a reversible strain of more than 3 % still compares well with other references for nanoporous palladium<sup>[4]</sup>. The attained maximum elongation for alloy B (80/20at% - compare Fig.4.5) of 1.7% is the lowest value of the three different initial stoichiometries, which can be explained by the (mechanical) failure already during the loading process. Comparing electrocapillary coupling coefficients the highest values of 1.9 V at lower hydrogen concentrations and 5.4 V at higher concentrations could be obtained for alloy B (80/20at%). In other words, the charge necessary for a certain actuation is the smallest in samples from alloy B.

Table 5.2: Actuator properties of nanoporous samples from different master alloys

$C$  . . . . . composition

$(\frac{\Delta\epsilon_{\max}}{\Delta c_f})_i$  . . . strain-coefficients - slopes of the fitted lines in Fig.4.5

$\zeta_i$  . . . . . electrocapillary coupling coefficient calculated according to Eq.5.3

$\epsilon_{\max}$  . . . . . maximum elongation

$C$	$(\frac{\Delta\epsilon_{\max}}{\Delta c_f})_1$	$\zeta_1 / \text{V}$	$(\frac{\Delta\epsilon_{\max}}{\Delta c_f})_2$	$\zeta_2 / \text{V}$	$\epsilon_{\max} / \%$
80/20wt% (A1)	1.4	1.0	6.6	4.9	3.1
80/20at% (B4)	2.5	1.9	7.3	5.4	1.7
75/25at% (C1)	1.7	1.3	6.2	4.6	2.1

Viswanath and Weissmüller<sup>[43]</sup> introduced a model for the hydrogen sorption strain and derived theoretical values for the electrocapillary coupling coefficients for hydrogen ad- and absorption of 1.17 V and 4.9 V. Those values were in agreement with their experimental results of electrochemical hydrogen loading on consolidated palladium nanoparticles in NaF solution and are also in accordance with the two different electrocapillary coupling coefficients determined for nanoporous samples in the present work.

It might as well be possible to distinguish the present palladium hydride phases in the concentration-strain diagrams (Fig.4.5), but due to the limited number of data points a phase characterisation is restricted to voltage-dependent measurements in this thesis (see Sec.5.2).

To support the values for the electrocapillary coupling coefficients determined from potentiostatic experimental data, the two slopes were linked to strain-charge curves originating from cyclic voltammetry measurements (see Sec.4.5). Therefore strain values were scaled with a mass-dependent factor according to Eq.5.2 and plotted over charge in Fig.5.1. The slopes of the lines added in the graphs represent electrocapillary coupling coefficients from Tab.5.2. The y-axis offset of the lines was chosen arbitrarily to fit experimental data.

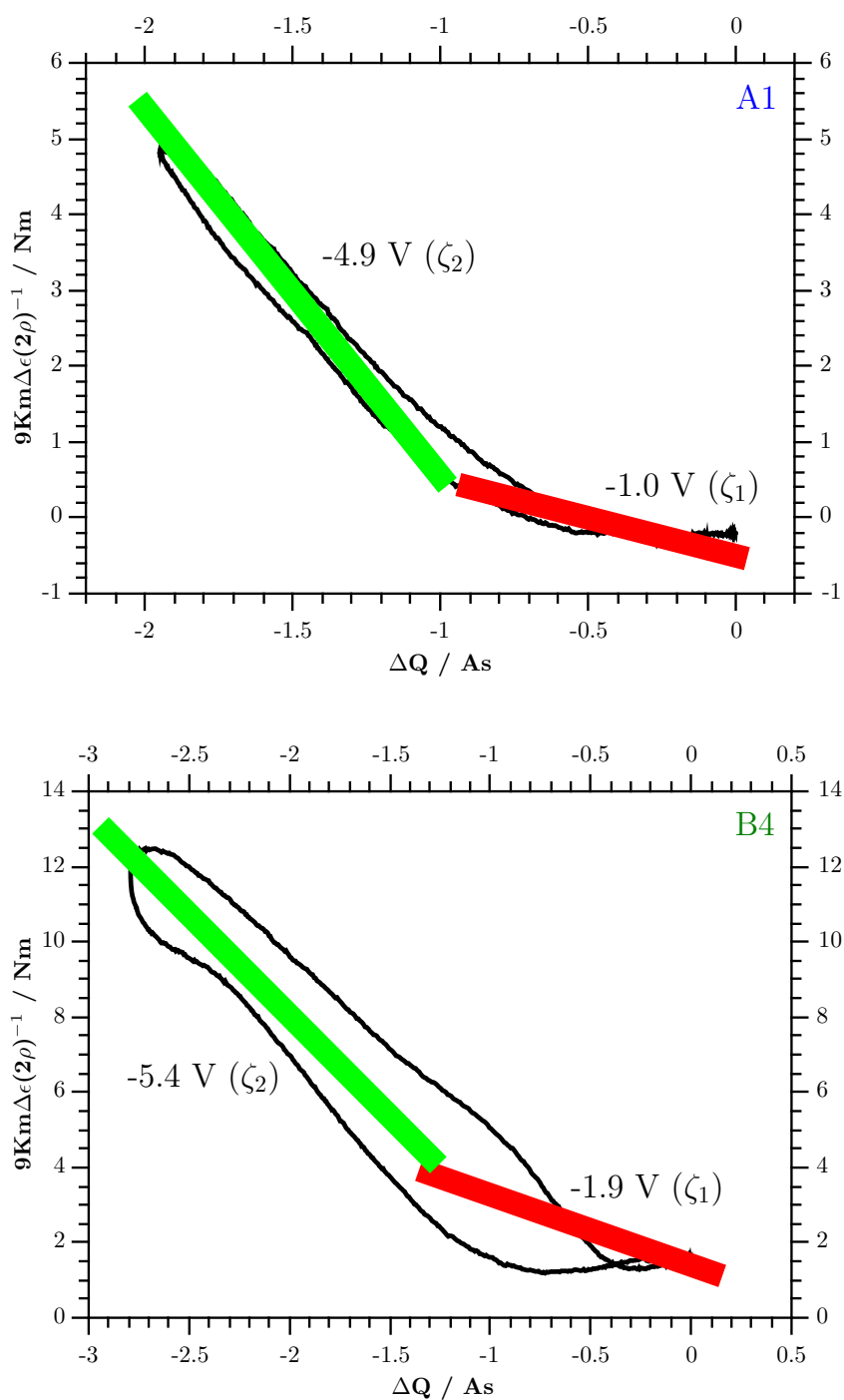


Figure 5.1: Values for  $9Km\Delta\epsilon(2\rho)^{-1} = -\zeta\Delta Q$ , according to Eq.5.2, versus charge  $\Delta Q$  for a single voltammetric cycle in 1 M KOH for samples A1, B4 and C1 (see inset). Zero on both axes was chosen at  $-0.5 \text{ V}$ , scan rate  $0.5 \text{ mVs}^{-1}$ . The y-offset of the coloured lines was chosen arbitrarily, numbers indicate corresponding slopes ( $\zeta$ -values)

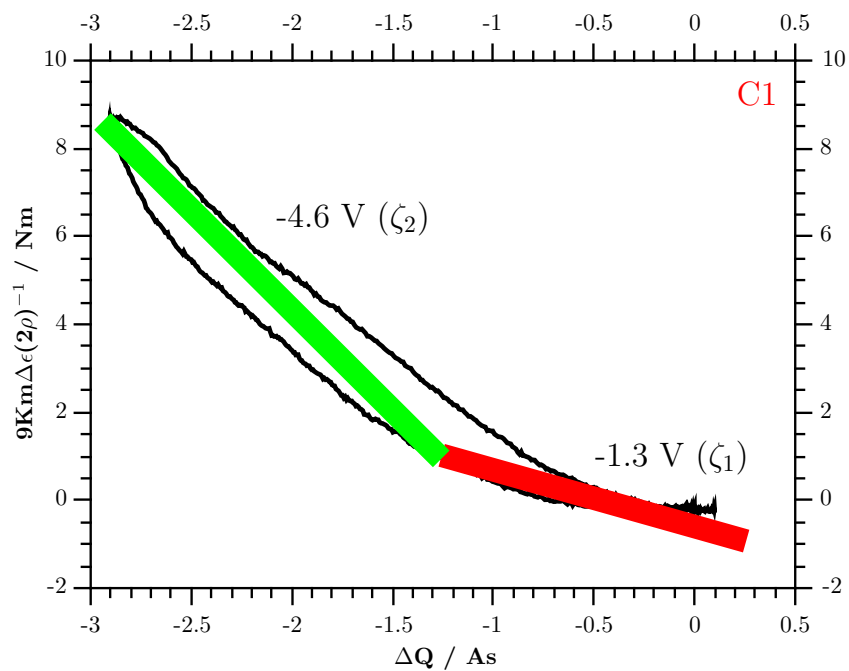


Figure 5.1: continuation from previous page

Coloured lines in Fig.5.1, representing electrocapillary coupling coefficients determined from potentiostatic measurements, were generally in good agreement with the strain-charge behaviour during voltammetric cycling in the hydrogen regime.

## 5.4 Anomalous Behaviour of Samples from Alloy D

The most puzzling finding within the scope of this thesis is the strain behaviour upon hydrogenation of nanoporous palladium from alloy D (CoPd70/30at%). While nanoporous samples from initial alloys with higher cobalt fractions expand reversibly in the electrochemical hydrogen regime in 1M KOH, samples from this special composition contract reversibly in the same voltage range (see Fig.4.3, Fig.4.5 or Fig.4.8). Comparing results from cyclic voltammetry (Sec. 4.5) with literature findings, three samples (A1, B4 and C1) are in accordance to plots presented in a recent work of Steyskal et al. [2], whilst sample D1 (CoPd70/30at% alloy) showed entirely different behaviour. For the former three samples a reduced strain hysteresis compared to strain-voltage-plots could be observed, which agrees with literature data<sup>[43]</sup> for palladium nanoparticles. The CoPd70/30at% sample (D), however, shows an amplified hysteresis loop starting at potentials smaller than -0.35 V with an inverted slope compared to the other master alloy stoichiometries. In order to find explanations for this effect, the intrinsic differences of the alloys should be taken into account.

Considering the phase diagram of the palladium-cobalt system, one recognises two different phases separated by a narrow miscibility gap (see. Fig.5.2). The cobalt-rich phase forms a hcp cobalt lattice with interstitial palladium atoms. The palladium rich phase is a solid solution of palladium and cobalt atoms in a fcc structure. From the (experimental) phase diagram it is not possible to determine the concentration range of the miscibility gap at room temperature, as the phase diagram is not plotted in that region. Nonetheless, it is certainly possible that the border of the single phase hcp region and the two-phase area is located between 75 at% and 70 at% of cobalt.

A different crystallographic structure of cobalt-palladium alloys is likely to behave differently during the dealloying process and form an altered porous structure, as shown for different gold-aluminium phases by Zhang et al. [44]. In their work they show, that different nanoporous structures form locally, dependent on the phase of a two-phase AlAu master alloy. For the palladium-cobalt system this statement is supported by the SEM measurements conducted on samples after dealloying (Sec.4.8). The structure in Fig.4.16 differs from the nanoporous network formed from other initial alloys (e.g. Fig.4.13) and does also vary locally on the sample surface. Samples from CoPd75/25at% alloys may possess a hierarchical structure (Fig.4.14), which could be a result from the presence of two CoPd phases in the master alloy. However, XRD-measurements contradict this explanation, as all XRD patterns, regardless of composition, showed single peaks between pure palladium and cobalt, indicating

the formation of homogeneous solid solutions. Still, the idea should not be rejected out of hand, as the technique of electron beam melting cannot exclude different local compositions. The sample surface, as scanned by the XRD, could be a homogeneous one-phase region, but the bulk could also contain more than one phase.

The effect of a negative reversible strain may be connected with structural factors. A structural phase-transition might occur during hydrogen loading in sample D, leading to a closer packing and a thinning of the sample in the corresponding potential region. There are reports on a reduction of the lattice parameter of palladium hydride with the appearance of a high vacancy phase at high temperatures and pressures<sup>[45,46]</sup>. However, the formation of this phase is not very likely, as the experimental conditions to stabilise this phase in the above-mentioned works differ vastly from the conditions in the present thesis. Although this phase transition leads to a reduction of the lattice parameter the total sample thickness would probably still increase due to excess palladium atoms in the new phase. Another interesting publication which might give a possible explanation for the negative reversible strain in nanoporous palladium sample from alloy D was published by Hakamada et al.<sup>[47]</sup>. They measured pressure-composition isotherms of nanoporous platinum samples and discovered an anomalous hydrogen release at high pressures. They attribute this behaviour to the relaxation/preservation of lattice strains in nanoporous platinum. The effect in the present nanoporous palladium samples could be related to their finding, as platinum and palladium exhibit similar properties. One fact contradicting this explanation is the charge balance, which points towards hydrogen absorption (a negative charge flow) at low voltages for samples from alloy D too.

The issue of the negative reversible strain remains unsolved at this point. The possible explanations, being a palladium hydride phase transition and the relaxation/preservation of lattice strains, require further investigation in future studies. Advanced structural characterisation, e.g. by transmission electron microscopy, might provide new insights to this question.

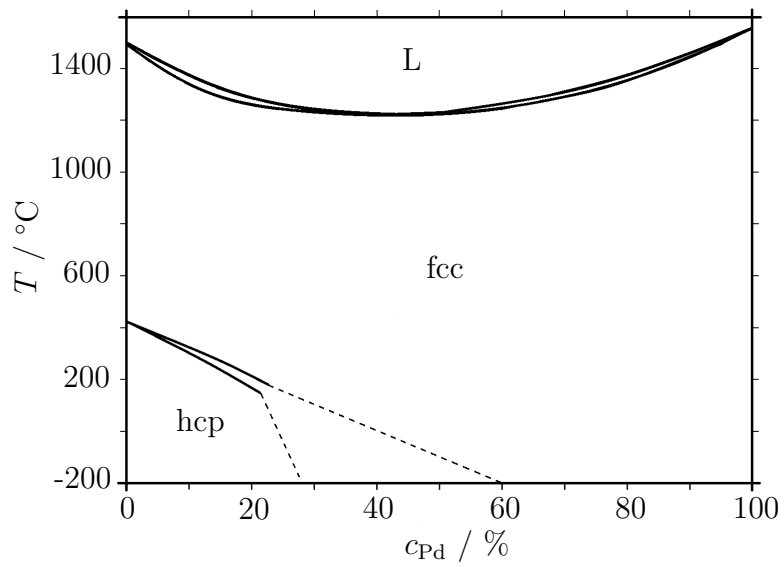


Figure 5.2: Schematic phase diagram of cobalt-palladium,  $c_{\text{Pd}}$  denotes the palladium concentration, range of the miscibility gap is unknown for the dashed region

## 5.5 Palladium Electrodeposition and Irreversible Strain

In the CVs, especially in acidic media and potassium chloride solution (Fig. 4.12) in section 4.7 three different contributions to the irreversible length changes during cyclic voltammetric measurements were identified (roman numerals in the graphs), which shall be discussed in this section. Underlying (electro-)chemical reactions necessary to understand palladium electrodeposition in different electrolytes were outlined in section 2.

- Anodic palladium dissolution could be identified as the reason for the contribution in the high potential regime (Process **III** in Fig.4.12). This effect has been investigated in literature via quartz crystal microbalance studies<sup>[48,49]</sup> in acidic electrolytes. The frequency changes in the publication of Grdeń et al.<sup>[48]</sup> show striking similarities with the length changes measured in the present work in a comparable potential window. This process is accompanied by a decrease in electrode mass and leads to severe damaging of the sample.
- Process **II** was assigned to chloride ion assisted dissolution of palladium<sup>[35]</sup>. The peak in the palladium CV in 1 M KCl solution between -0.3 V and 0 V, attributed to  $\text{Cl}^-$ -complex formation, coincides with the interval of the length changes. The chemical foundation can be found in section 2. This process also involves a decrease in electrode mass and sample degradation, consequently.
- The length changes related to process **I** have not been explained in literature so far. The process of hydrogen ad- and absorption, which is supposed to take place in the same potential regime, was expected to expand reversibly, as samples in KOH (Sec.4.3, Fig.4.3). The uptake of hydrogen atoms in the sample bulk and at the sample surface respectively, is responsible for the expansion in KOH. For thin palladium layer electrodes this was measurable as a reversible change of frequency, and thus mass, of a quartz crystal microbalance<sup>[48]</sup>.

However, no irreversible changes of mass were detected in the mentioned work<sup>[48]</sup> in the hydrogen region, which lead to the assumption another mechanism than bulk palladium dissolution is responsible for process **I**. The present effect of a continuous decrease in length in acidic electrolytes in the hydrogen regime for nanoporous palladium was first reported by Zhang et al.<sup>[3]</sup> in  $\text{H}_2\text{SO}_4$ . In this work their findings could be confirmed, although minor differences in data interpretation exist. It is suggested that the irreversible decrease in length vanishes after a sufficiently large number of cycles

and a reversible actuation behaviour similar to that in KOH ensues. Measurements in  $\text{HClO}_4$  (as for example in Fig.4.12-B6) indicate that the reversible actuation behaviour is still present as a superimposed strain, but is dominated by the stronger irreversible effect. Still, the predicted long-term behaviour should be verified experimentally by prolonged measurements in acidic electrolytes.

In the following important concepts in order to understand the length changes associated with process I above are introduced, with two possible explanations (a) and (b) being presented at the end.

It is established in literature that hydrogen can alter the mechanical properties of palladium<sup>[50][51]</sup>. An effect called "Hydrogen enhanced localised plasticity" has been reported to cause a softening of the material<sup>[52]</sup>. The hydrogen atoms are supposed to enhance dislocation mobility, especially in small-grained, high-defect structures. On the other hand hydrogen embrittlement is a well-known process occurring in many metal-hydrogen systems<sup>[53–55]</sup>. In order to illustrate this process, a schematic from the publication of Hongo et al.<sup>[50]</sup> has been included in this work (see Fig.5.3). In this mechanism the inclusion of hydrogen atoms causes a strain and induces the formation of dislocations in the metal, impeding overall dislocation movement and hardening the metal. This process is comparable to work hardening, in this case induced by hydrogen absorption.

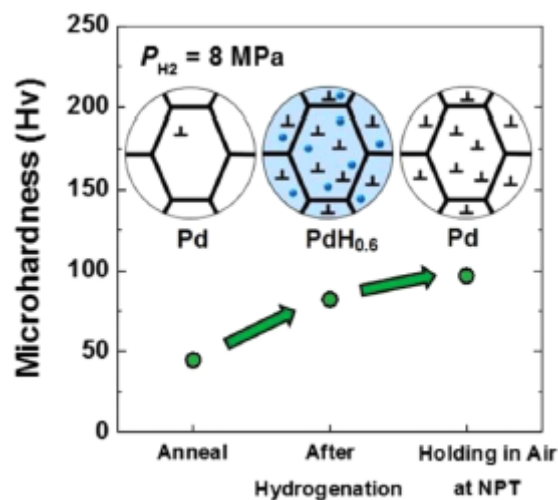


Figure 5.3: Schematic representation of the hydrogen embrittlement mechanism. Hydrogen atoms are indicated as blue dots, the hydride phase is shaded blue. NPT is an abbreviation for Normal Pressure and Temperature. Image reprinted from Hongo et al.<sup>[50]</sup> with permission from Elsevier

Although both mechanisms, hydrogen enhanced localised plasticity and hydrogen embrittlement, can help explaining the mechanical properties of the nanoporous palladium-hydrogen system and thus the measured strain curves to some extent, they do not provide any obvious reason for the absence of the irreversible strain in KOH solution on their own. Irreversible shrinkage during voltammetric cycling in the hydrogen regime was only observed in acidic electrolytes.

When focusing on the differences of the loading and the unloading processes the different loading and unloading kinetics have to be considered. As introduced in Sec.2.4 the adsorption and desorption of hydrogen atoms do not necessarily follow the same chemical mechanism<sup>[56]</sup>. A summary of all possible hydrogen sorption processes can be found in Fig.5.4. As there are more available reactions during desorption it is reasonable to assume that the desorption process is faster compared to ad- and absorption. For a quantitative assessment the rate constants of all reactions in Fig.5.4 would have to be determined, which goes beyond the scope of the present thesis. However, the effect has been observed by different authors<sup>[31,32]</sup> in practical experiments. Gabrielli et al.<sup>[31]</sup> states that the desorption process is fast and accompanied by a decrease in volume of the electrode and a relaxation of the palladium crystal lattice. It should be noted that kinetics of hydrogen sorption does also change in different electrolytes. From a purely chemical standpoint the higher concentration of H<sup>+</sup>-ions in acid shifts the equilibrium in equation 2.2 to the right and enlarges the rate constant in that direction. In experiments in this work it was found that not only the adsorption process, but also the desorption process is faster in acidic electrolytes in samples from alloys A, B and C. This could be evaluated by comparing charging curves and corresponding elongations in acid and base.

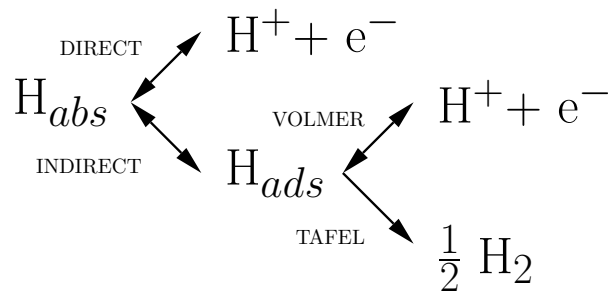


Figure 5.4: Schematic of the different possible sorption mechanisms of hydrogen into palladium, For chemical details see Sec.2

Two different explanations for the irreversible shrinkage in the hydrogen regime, both based on the sorption kinetics, will be discussed in the following. The first one addresses the difference in hydrogen concentration profiles in a ligament during loading and unloading (a), while the latter utilises a strain-rate dependence of mechanical properties (b).

(a) **Ligament concentration profiles:**

Based on the assumption that absorption is generally faster than diffusion, different concentration profiles in the ligaments of nanoporous palladium in acid and base can be expected for different reaction kinetics. A verification of this premise would be possible for known rate-constants of the palladium ad- and absorption reactions, as diffusion constants are well-known in literature<sup>[57]</sup> for both phases ( $D_\alpha = 1.6 \cdot 10^{-7} \text{ cm}^2\text{s}^{-1}$ ,  $D_\beta = 1.5 \cdot 10^{-6} \text{ cm}^2\text{s}^{-1}$ ). Diffusion in the palladium hydride  $\beta$ -phase proceeds one order of magnitude faster than in the  $\alpha$ -phase. An illustration for the following explanation can be found in Fig.5.5. At the beginning of a charging experiment surface-near regions of nanoporous palladium can be considered to be rich in hydrogen compared to the ligament core. This concentration difference amplifies for measurements in acidic media. After sufficiently long times the concentration profiles should become uniform (Fig.5.5 - left).

At the beginning of unloading experiments, after a full hour of loading, the concentration profile of the system can be assumed to be on a constant level. The surface-near regions then get depleted with advancing unloading, reaching an inverse concentration gradient compared to the loading process (Fig.5.5 - right). Translating this into strain, a hydrogen-rich strained core is surrounded by a shell of contracted palladium. This causes an internal stress, which could support the explanation of the irreversible length changes in nanoporous palladium samples.

(b) **Strain-rate dependent mechanical properties:**

Higher reaction rates of hydrogen ab- or desorption do also imply higher strain-rates as the inclusion of hydrogen atoms causes a direct widening of the crystal lattice. Therefore a strain-rate dependency of the mechanical properties could be a possible explanation for the irreversible strain associated with process **I** above.

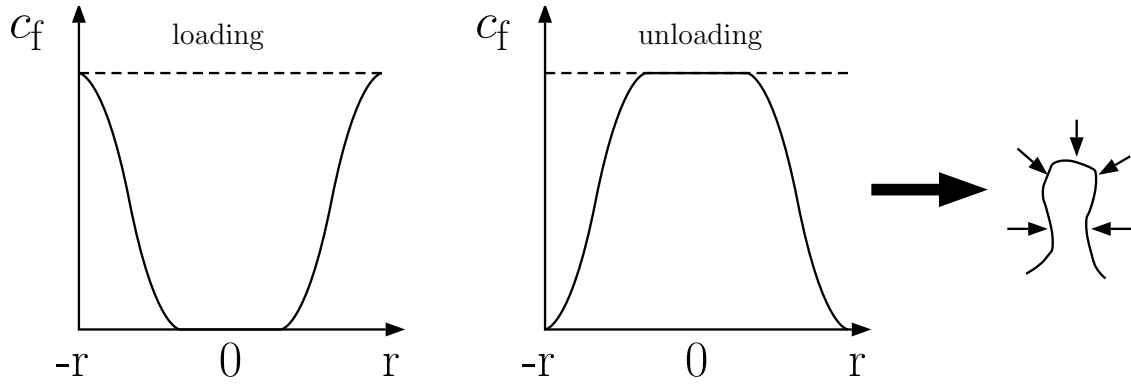


Figure 5.5: Schematic illustration of the concentration profiles across one single symmetric ligament during loading and unloading,  $c_f$  denotes the hydrogen concentration, while  $r$  is the distance from the ligament centre to the surface. The unloading process can impose an internal strain to the ligament core.

A generalised description of a strain-rate sensitive material is given by the equation<sup>[58]</sup>

$$\sigma = k\dot{\epsilon}^m \quad (5.4)$$

where  $\sigma$  denotes the flow stress,  $k$  a proportionality constant,  $\dot{\epsilon}$  the strain-rate and  $m$  the strain rate sensitivity.

The mechanical properties of nanoporous gold have been studied in the work of Jin et al.<sup>[18]</sup>. They reported a significant strain-rate-sensitivity in compressive stress-strain-curves at high strains, an increasing strain rate leads to higher values for the yield strength and thus better mechanical stability in their work<sup>[18]</sup>. Soare and Curtin showed in their comprehensive theoretical model for fcc metals that negative values for the strain-rate-sensitivity  $m$ , and softening of the material at high strain rates, are only possible if more than one rate-dependent strengthening mechanism is present in the material. Besides the process of dislocation strengthening another mechanism, e.g. interactions of dislocation junctions with solute atoms, has to interfere. This points towards hydrogen atoms as important contributors to this effect. To illustrate the effect of a negative strain rate sensitivity a schematic of two different stress-strain curves is depicted in Fig.5.6. In the paper of Bal et al.<sup>[54]</sup> a negative strain-rate-sensitivity  $m$  was reported for hydrogen-treated fcc-steel. They explain this by a promotion of hydrogen embrittlement due to hydrogen-dislocation interaction at low strain rates. This mechanism seems also applicable for palladium hydride.

In this context it should be mentioned that regardless of initial alloy composition an excess charge emerged in the unloading experiments when the samples yielded.

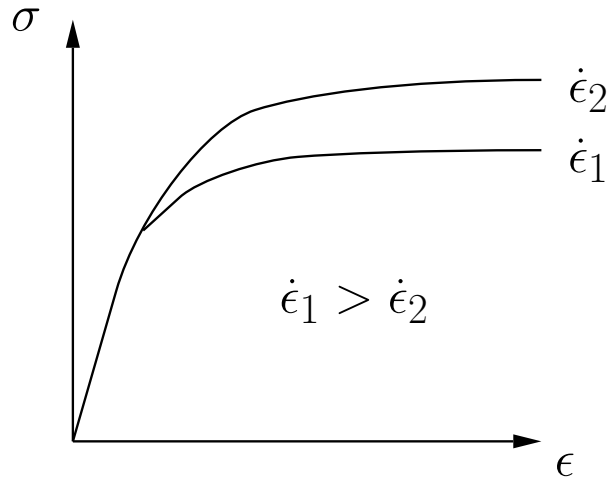


Figure 5.6: Schematic illustration of a negative strain-rate sensitivity using stress( $\sigma$ )-strain( $\epsilon$ )-curves,  $\dot{\epsilon}_i$  denotes a certain strain rate  $i$

In general charges during loading and unloading were equal except for a small offset attributed to hydrogen evolution. The additional charge in the order of several As could emerge from the dissolution of residual cobalt in the nanoporous structure, which is exposed to the electrolyte after the sample fractures. The unloading potential in the double layer regime would definitely allow cobalt dissolution ( $E^0=0.277\text{ V}^{[60]}$ ) in both acidic and alkaline media. It is supposed that the force of the dilatometer pushrod of 100 mN applied to the sample in connection with the strain rate induced softening of the palladium hydride alloy is enough to cause fracture. This does not only affect strain during cyclovoltammetric measurements, but also during loading experiments at constant potentials (compare section 4.4) in the hydrogen regime.

To support the explanation proposed including a strain-rate sensitive deformation, the strain rates were estimated for different charging processes via the electrochemical discharging current. As explained above, more than one single mechanism is available for hydrogen desorption, but the maximum current of an unloading experiment per unit mass seemed reasonable as a first estimate of the strain rate. The current can be assumed to be proportional to the incorporation rate of hydrogen atoms in the lattice and thus the rate of expansion in a simple picture. The currents, which are compared, refer to the unloading currents of the experiment when the sample fractured and the preceding unloading measurement (at potentials of -1.0 V and -0.95 V in KOH and -0.2 V and -0.15 V in perchloric acid). The calculated values for estimated strain rate for samples from alloys A, B and C are presented in Tab.5.3.

Table 5.3: Calculated strain rate estimates as unloading peak currents per palladium mass for different samples

$C$  ..... Composition

$I_1$  ..... Peak unloading current after preceding polarisation at -1 V

$I_2$  ..... after preceding polarisation at -0.95 V

$\frac{I_1}{m}$  ..... Peak unloading current per sample mass at sample fracture (-1 V)

$\frac{I_2}{m}$  ..... Peak unloading current per sample mass before sample fracture (-0.95 V)

$C$	electrolyte	$I_1 / \text{mA}$	$I_2 / \text{mA}$	$\frac{I_1}{m} / \text{mAg}^{-1}$	$\frac{I_2}{m} / \text{mAg}^{-1}$
75/25at%	KOH	49	41	1670	1400
75/25at%	HClO <sub>4</sub>	60	40	1950	1300
80/20at%	KOH	48	34	2240	1580
80/20wt%	KOH	38	32	2790	2350
80/20wt%	HClO <sub>4</sub>	31	23	2280	1690

Estimates for  $\dot{\epsilon}_1$ , the strain rate at the unloading step at which the sample yields ( $\frac{I_1}{m}$ ), and  $\dot{\epsilon}_2$ , the strain rate before sample fracture ( $\frac{I_2}{m}$ ) can be found in Tab.5.3.

Comparing these values no universal value for the peak current per mass could be determined at which the nanoporous palladium samples fracture. It is very likely that other desorption paths (especially Tafel recombination - the non-electrochemical desorption pathway in Fig.5.4) have a greater contribution to the total discharging process. It is assumed that no universal strain rate of palladium fracture can be defined, as different initial alloys and thus microstructures do influence the material strength. On the other hand the model of a current per mass as an estimation for strain rate might be too simplistic and other factors such as specific surface area should be included.

In order to understand the mechanism of palladium electrodisolution one should be familiar with chemical reactions of palladium, which are presented in section 2. Several ions have been reported to enhance palladium electrodisolution<sup>[33]</sup>, including ClO<sub>4</sub><sup>-</sup>, H<sub>2</sub>SO<sub>4</sub><sup>-</sup> and Cl<sup>-</sup>, which are present in electrolytes in the current work. In Cl<sup>-</sup>-containing solutions reaction 2.9 describes one sample formation of a soluble Pd-complex and reaction 2.10 the corresponding precipitation, which is a direct dissolution pathway. In sulfuric and perchloric acid solution the situation is more complex, different mechanisms are proposed in literature<sup>[33]</sup>. Palladium oxide or palladium hydroxide (formed according to Eq.2.6 and 2.7) can act as precursors for dissolution and take part in complex formation with HSO<sub>4</sub><sup>-</sup> and ClO<sub>4</sub><sup>-</sup>. Alternatively a weakening of the palladium surface bonds is proposed as solution. In general dissolution is more pronounced in acidic electrolytes compared to basic ones. As the rate-limiting step in palladium electrodisolution is electrolyte diffusion, the scan rate in cyclovoltammetric measurements has a direct influence on the dissolution rate.

## 5.6 Correction for the Irreversible Strain

Measurements of length changes during cyclic voltammetry in all electrolytes were subject to a certain irreversible, negative cycle-to-cycle offset, attributed to chemical (dissolution) reactions. The magnitude of this strain drift was generally large in acidic electrolytes and potassium chloride solution, as dissolution is promoted (see Sec.5.5, Fig.4.12), and comparably small for measurements in potassium hydroxide solution (see Sec.4.3, Fig.4.3). In order to enable better comparability of strains corresponding to reversible processes, especially hydrogen absorption, a linear drift correction was applied. Therefore peaks associated with hydrogen absorption were chosen as reference points, which were forced on the same level by adding the total cycle offset (measured from peak to peak) proportionally to each single value in the interval between the two peaks. The correction method is illustrated in Fig.5.7 for one exemplary measurement on sample A1 in 1M KOH plotted over time. The sharper peak is associated with hydrogen absorption, while the broader (double-)peak appears in the potential region of oxide formation.

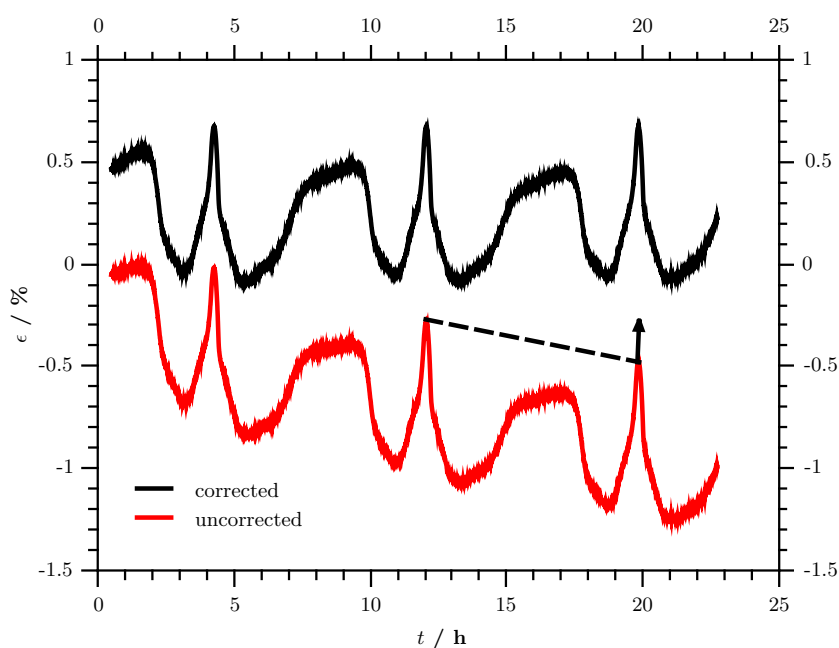


Figure 5.7: Illustration of the linear strain correction, strain  $\epsilon$  as a function of time  $t$  for sample A1 during voltammetric cycling (scan rate  $0.1\text{mVs}^{-1}$ ) at potentials between  $-1\text{V}$  and  $0.4\text{V}$  in  $1\text{M KOH}$ . A linear correction was applied to the black curve, while the red curve displays the uncorrected behaviour. Corrected curve shifted by a constant value on the strain axis in order to enable comparability. Dashed line and arrow indicate the correction for one cycle.

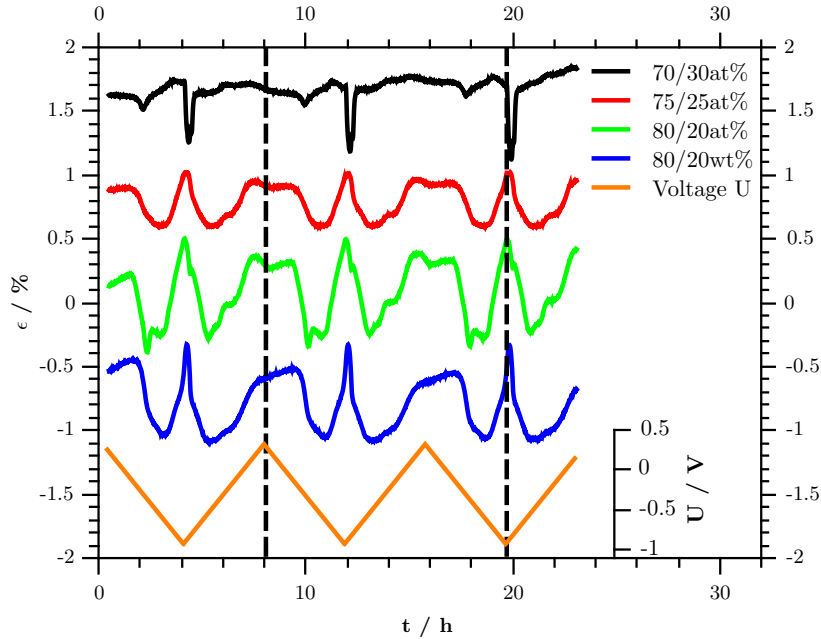


Figure 5.8: Strain  $\epsilon$  as a function of time  $t$  for nanoporous samples from four initial compositions during voltammetric cycling (scan rate  $0.1\text{mVs}^{-1}$ ) at potentials between  $-1\text{V}$  and  $0.4\text{V}$  in  $1\text{M KOH}$ . A linear correction was applied to correct the curves for an irreversible contribution. Curves shifted by constant values on the strain axis in order to enable comparability. Corresponding voltage is shown on the inset axis. The dashed lines serve as guides to the eye.

Evidently, such a correction has its limitations. As different chemical reactions may contribute to a higher or lower extent to the overall drift, a linear estimation of the strain offset does not compensate for the drift accurately. Nonetheless, reasonable results were obtained for measurements in  $1\text{M KOH}$  solution. An exemplary plot of corrected strain versus time during a CV measurement in  $\text{KOH}$  at a scan rate of  $0.1\text{ mVs}^{-1}$  is depicted in Fig.5.8 for samples from all initial stoichiometries. The simplistic linear correction is stretched to its limits when applied to measurements in acidic media. This becomes apparent in the double layer regime, where regardless of the electrolyte used for the experiment no (significant) degradation takes place. Therefore an averaged linear drift correction gives a certain overcompensation in this potential range. In  $\text{KOH}$  solution, where the overall drift is small, this overcompensation is negligible. However, for the experiments in acid the drift correction leads to a severe overcompensation and therefore a strongly distorted signal in the range of the double layer, due to the much higher dissolution rates in other regimes. A more advanced approach would include a stepwise linear correction, considering chemically inactive regions in the CV as well as distinct dissolution peaks. This method might also be applicable

to measurements in potassium chloride solution, as dissolution occurs in well-separated steps (compare Fig.4.12-B2). A correction for the irreversible strain without any simplifications would include electrochemical calculations of dissolution rates and require knowledge of the diffusion coefficients of palladium ions in the respective electrolyte. Furthermore, any correction should be limited to a certain potential range, as otherwise overcorrections might occur again in the double layer regime.

## 5.7 Nanoporous Palladium as Energy Storage Medium

The potential benefits of palladium as solid state hydrogen storage can be easily shown by estimating the energy density of palladium hydride. Assuming no losses during charging and discharging and a controlled oxyhydrogen combustion, which is the reaction taking place in fuel cells, the specific energy per unit mass can be calculated using Eq.5.5.

$$\begin{aligned} \frac{E}{m} &= \frac{m_{\text{Pd}}}{M_{\text{Pd}}} \cdot c_{\text{f}} \cdot \frac{1}{(m_{\text{Pd}} + m_{\text{H}})} \cdot \frac{1}{2} \cdot \Delta H \cdot \eta \\ &\approx \frac{c_{\text{f}} \cdot \Delta H}{2M_{\text{Pd}}} \cdot \eta \\ &= 472 \frac{\text{kJ}}{\text{kg}} \end{aligned} \quad (5.5)$$

$\frac{E}{m}$  ..... Energy density

$m_{\text{Pd}}$  ..... Palladium mass

$M_{\text{Pd}}$  ..... Molar mass of palladium, 0.106 kg

$c_{\text{f}}$  ..... Atomic hydrogen concentration H: Pd, 0.7 as reached in experiments in this work

$m_{\text{H}}$  ..... Hydrogen mass

$\Delta H$  ..... Molar reaction enthalpy of hydrogen combustion, 285.8 kJ/mol

$\eta$  ..... Process efficiency, assumption: 50 %

The energy density is estimated by calculating the number of moles of hydrogen atoms  $\frac{m_{\text{Pd}}}{M_{\text{Pd}}} \cdot c_{\text{f}}$  times half the molar reaction enthalpy for combustion of gaseous hydrogen  $\Delta H$ . This energy value is divided by the total sample mass  $m_{\text{Pd}} + m_{\text{H}}$  and multiplied with a device efficiency  $\eta$ . Sample masses cancel out assuming  $m_{\text{Pd}} \simeq m_{\text{Pd}} + m_{\text{H}}$ . For the device efficiency a value of 50% was assumed, which is typical for fuel cells. This estimated value of  $\sim 470$  kJ/kg is comparable with the energy densities of lithium-ion-batteries ( $\sim 430$  kJ/kg<sup>[61]</sup>) and well-above experimental values for lead-acid-batteries ( $\sim 130$  kJ/kg<sup>[61]</sup>). Although this value compares favourably with batteries, fossil fuels reach energy densities of about two orders of magnitude higher (40-50 MJ/kg)<sup>[62]</sup>. Light-weight metals hydrides as magnesium hydride  $\text{MgH}_2$  can reach energy densities about one order of magnitude higher than PdH, although technical realisation and high heats of desorptions remain a challenge to overcome<sup>[63]</sup>.

Two dominant factors discouraging from using palladium as energy storage in practice are both the large strains (up to 3% in this work) upon hydrogen inclusion and the high price of

palladium. Nonetheless, palladium based materials<sup>[6]</sup> could still play a role in future hydrogen storage. Pure palladium remains a popular model system to investigate mechanisms of solid state hydrogen storage. State of the art research in materials-based hydrogen storage still focuses partly on (light) hydride materials due to high storage densities (larger than in liquid hydrogen<sup>[64]</sup>) and a reliable long-term retention. Their inferior ab- and desorption kinetics<sup>[64]</sup> still leave a lot of scope for improvement. Porous materials as hydrogen storage are always on the cards, due to the generally improved hydrogen storage with high surface areas. Materials with specific surface areas of more than  $2000 \text{ m}^2\text{g}^{-1}$  were investigated in the literature<sup>[64]</sup>. Further reasearch fields include hydrogen storage in its para-form or storage in ionic liquids<sup>[64]</sup>.

# Chapter 6

## Conclusion

Within the scope of this thesis nanoporous palladium samples were produced by dealloying and studied with respect to their hydrogen-loading behaviour. For this purpose four different cobalt-palladium master alloys (CoPd70/30at%, 75/25at%, 80/20at% and 88/12at%) were produced by electron-beam-melting in cooperation with the Institute of Materials Science and Welding at TU Graz. Alloys were rolled and thinned into 250-270  $\mu\text{m}$  thick foil and cut into 5x5 mm<sup>2</sup> squares. The dealloying process was examined with regard to cobalt content, charge flow and duration.

In order to investigate hydrogen storage and actuation properties a combined electrochemical and dilatometric measurement was conducted in-situ in different electrolytes (KOH, KCl, H<sub>2</sub>SO<sub>4</sub>, HClO<sub>4</sub>). Samples were placed under the pushrod of a dilatometer as working electrode in an electrochemical cell. This allowed the determination of strains corresponding to certain electrochemical reactions. Focus was put on characterisation in the hydrogen regime with both cyclovoltammetric and chronoamperometric studies in 1 M KOH and 0.5 M HClO<sub>4</sub>.

A maximum reversible expansion of about 3% was reached for potentiostatic loading in KOH at a hydrogen concentration of 0.6 H:Pd. A high contribution of adsorbed hydrogen to the total hydrogen concentration was observed during potentiostatic measurements at high loading potentials in KOH, which is attributed to the high specific surface areas of nanoporous palladium. Strain versus charge and concentration versus potential plots were included to proof the presence of two different palladium hydride phases in nanoporous palladium samples.

For nanoporous samples from the CoPd70/30a% alloy an anomalous contraction was measured in the potential region where hydrogen uptake is supposed to happen. This effect was present in multiple samples prepared from that alloy and found in both chronoamperometric and cyclic voltammetric measurements. The reason for it remains unclear, different cobalt-palladium phases in the master alloy could be a possible explanation.

Moreover, unexpected mechanical failure was observed during unloading from high hydrogen contents in both KOH and HClO<sub>4</sub> solutions. This effect was more pronounced in acidic media and has not been reported in literature so far. Strain-rate dependent mechanical properties are suggested as a possible explanation. Measurements in 0.5 M H<sub>2</sub>SO<sub>4</sub> and 1 M KCl were found to cause palladium dissolution in certain potential regions and lead to an irreversible reduction in sample length.

In addition, the specific surface area was determined for samples from all initial stoichiometries via two different electrochemical methods in 0.5 M H<sub>2</sub>SO<sub>4</sub>, with typical values in the order of 15 m<sup>2</sup>g<sup>-1</sup>. One utilised the double layer capacitance, while the second is based on charge associated with the formation of the first palladium oxide monolayer. Furthermore SEM images were recorded for nanoporous palladium samples at the Austrian Centre for Electron Microscopy and Nanoanalysis. Pore sizes were in the range of 5-20 nm, close to the limiting resolution of the electron microscope.

# Bibliography

- [1] R. WÜRSCHUM. Nanostructures and Nanotechnology, lecture script (2010).
- [2] E.-M. STEYSKAL, C. WIEDNIG, N. ENZINGER and R. WÜRSCHUM. In situ characterization of hydrogen absorption in nanoporous palladium produced by dealloying. *Beilstein Journal of Nanotechnology*, **7** (2016) 1197. doi:10.3762/bjnano.7.110.
- [3] J. ZHANG, Y. WANG, C. SI, Q. BAI, W. MA, H. GAO and Z. ZHANG. Electrochemical actuation behaviors of bulk nanoporous palladium in acid and alkaline solutions. *Electrochimica Acta*, **220** (2016) 91. doi:10.1016/j.electacta.2016.10.091.
- [4] J. ZHANG, Q. BAI and Z. ZHANG. Dealloying-driven nanoporous palladium with superior electrochemical actuation performance. *Nanoscale*, **8** (2016) 7287. doi:10.1039/C6NR00427J.
- [5] B. D. ADAMS and A. CHEN. The role of palladium in a hydrogen economy. *Materials Today*, **14** (2011) 6 282. doi:10.1016/S1369-7021(11)70143-2.
- [6] S. K. KONDA and A. CHEN. Palladium based nanomaterials for enhanced hydrogen spillover and storage. *Materials Today*, **19** (2016) 2 100. doi:10.1016/j.mattod.2015.08.002.
- [7] P. TRIPODI, D. DI GIOCCHINO and J. D. VINKO. A review of high temperature superconducting property of PdH system. *International Journal of Modern Physics B*, **21** (2007) 18n19 3343. doi:10.1142/S0217979207044524.
- [8] H. M. SYED, C. WEBB and E. M. GRAY. Hydrogen-modified superconductors: A review. *Progress in Solid State Chemistry*, **44** (2016) 1 20. doi:10.1016/j.progsolidstchem.2016.02.001.

- [9] M. HAKAMADA and M. MABUCHI. Fabrication of nanoporous palladium by dealloying and its thermal coarsening. *Journal of Alloys and Compounds*, **479** (2009) 1–2 326. doi:10.1016/j.jallcom.2008.12.078.
- [10] L.-Z. LIU, X.-L. YE and H.-J. JIN. Interpreting anomalous low-strength and low-stiffness of nanoporous gold: Quantification of network connectivity. *Acta Materialia*, **118** (2016) 77. doi:10.1016/j.actamat.2016.07.033.
- [11] N. J. DUDNEY, W. C. WEST and J. NANDA. *Handbook of Solid State Batteries, 2nd edition*. World Scientific (2015).
- [12] W. SCHMICKLER and E. SANTOS. *Interfacial Electrochemistry 2nd edition*. Springer (2010).
- [13] J. BISQUERT, P. CENDULA, L. BERTOLUZZI and S. GIMENEZ. Energy diagram of semiconductor/electrolyte junctions. *The Journal of Physical Chemistry Letters*, **5** (2014) 1 205. doi:10.1021/jz402703d.
- [14] A. J. BARD, R. PARSONS and J. JORDAN. *Standard Potentials in Aqueous Solutions* (1985).
- [15] R. G. COMPTON and C. E. BANKS. *Understanding Voltammetry 2nd edition*. Imperial College Press (2011).
- [16] M. GRDEŃ, A. PIAŚCIK, Z. KOCZOROWSKI and A. CZERWIŃSKI. Hydrogen electro-sorption in Pd–Pt alloys. *Journal of Electroanalytical Chemistry*, **532** (2002) 1 35. doi:10.1016/S0022-0728(02)00750-7.
- [17] E.-M. STEYSKAL, M. BESENHARD, S. LANDGRAF, Y. ZHONG, J. WEISSMÜLLER, P. PÖLT, M. ALBU and R. WÜRSCHUM. Sign-inversion of charging-induced variation of electrical resistance of nanoporous platinum. *Journal of Applied Physics*, **112** (2012) 7 073703. doi:10.1063/1.4755808.
- [18] H.-J. JIN, L. KURMANAEVA, J. SCHMAUCH, H. RÖSNER, Y. IVANISENKO and J. WEISSMÜLLER. Deforming nanoporous metal: Role of lattice coherency. *Acta Materialia*, **57** (2009) 9 2665. doi:10.1016/j.actamat.2009.02.017.
- [19] F. NIU and Q. YI. A novel nanoporous palladium catalyst for formaldehyde electro-oxidation in alkaline media. *Rare Metals*, **30** (2011) 1 102. doi:10.1007/s12598-011-0248-y.

- [20] R. L. KERR, S. A. MILLER, R. K. SHOEMAKER, B. J. ELLIOTT and D. L. GIN. New type of li ion conductor with 3d interconnected nanopores via polymerization of a liquid organic electrolyte-filled lyotropic liquid-crystal assembly. *Journal of the American Chemical Society*, **131** (2009) 44 15972. doi:10.1021/ja905208f.
- [21] D. JALAS, L.-H. SHAO, R. CANCHI, T. OKUMA, S. LANG, A. PETROV, J. WEISSMÜLLER and M. EICH. Electrochemical tuning of the optical properties of nanoporous gold. *Scientific Reports*, **7** (2017) 44139. doi:10.1038/srep44139.
- [22] M. HAKAMADA, K. TAJIMA, K. YOSHIMURA, Y. CHINO and M. MABUCHI. Solid/electrolyte interface phenomena during anodic polarization of Pd<sub>0.2</sub>M<sub>0.8</sub> (M = Fe, Co, Ni) alloys in H<sub>2</sub>SO<sub>4</sub>. *Journal of Alloys and Compounds*, **494** (2010) 1–2 309. doi:10.1016/j.jallcom.2010.01.019.
- [23] L. L. JEWELL and B. H. DAVIS. Review of absorption and adsorption in the hydrogen-palladium system. *Applied Catalysis A: General*, **310** (2006) 1. doi:10.1016/j.apcata.2006.05.012.
- [24] F. D. MANCHESTER, A. SAN-MARTIN and J. M. PITRE. The H-Pd (hydrogen-palladium) system. *Journal of Phase Equilibria*, **15** (1994) 1 62. doi:10.1007/BF02667685.
- [25] J. A. EASTMAN, L. J. THOMPSON and B. J. KESTEL. Narrowing of the palladium-hydrogen miscibility gap in nanocrystalline palladium. *Phys. Rev. B*, **48** (1993) 84. doi:10.1103/PhysRevB.48.84.
- [26] G. JERKIEWICZ and A. ZOLFAGHARI. Comparison of hydrogen electroadsorption from the electrolyte with hydrogen adsorption from the gas phase. *Journal of The Electrochemical Society*, **143** (1996) 4 1240. doi:10.1149/1.1836623.
- [27] M. HAKAMADA, H. NAKANO, T. FURUKAWA, M. TAKAHASHI and M. MABUCHI. Hydrogen storage properties of nanoporous palladium fabricated by dealloying. *The Journal of Physical Chemistry C*, **114** (2010) 2 868. doi:10.1021/jp909479m.
- [28] R. GRIESSEN, N. STROHFELDT and H. GIESSEN. Thermodynamics of the hybrid interaction of hydrogen with palladium nanoparticles. *Nat Mater*, **15** (2016) 3 311.

- [29] R. K. SINGH, R. RAMESH, R. DEVIVARAPRASAD, A. CHAKRABORTY and M. NEER-GAT. Hydrogen interaction (electrosorption and evolution) characteristics of Pd and Pd<sub>3</sub>Co alloy nanoparticles: An in-situ investigation with electrochemical impedance spectroscopy. *Electrochimica Acta*, **194** (2016) 199. doi:10.1016/j.electacta.2016.01.231.
- [30] P. N. BARTLETT and J. MARWAN. The effect of surface species on the rate of H sorption into nanostructured Pd. *Phys. Chem. Chem. Phys.*, **6** (2004) 2895. doi:10.1039/B404028G.
- [31] C. GABRIELLI, P. P. GRAND, A. LASIA and H. PERROT. Investigation of hydrogen adsorption-absorption into thin palladium films: I. theory. *Journal of The Electrochemical Society*, **151** (2004) 11 A1925. doi:10.1149/1.1797033.
- [32] M. ŁUKASZEWSKI, K. KLIMEK, A. ZUROWSKI, T. KEDRA and A. CZERWIŃSKI. Kinetics and mechanism of hydrogen electrosorption in palladium-based alloys. *Solid State Ionics*, **190** (2011) 1 18. doi:10.1016/j.ssi.2010.03.009.
- [33] M. GRDEŃ, M. ŁUKASZEWSKI, G. JERKIEWICZ and A. CZERWIŃSKI. Electrochemical behaviour of palladium electrode: Oxidation, electrodisolution and ionic adsorption. *Electrochimica Acta*, **53** (2008) 26 7583. doi:10.1016/j.electacta.2008.05.046.
- [34] M. SHAO. Palladium-based electrocatalysts for hydrogen oxidation and oxygen reduction reactions. *Journal of Power Sources*, **196** (2011) 5 2433. doi:10.1016/j.jpowsour.2010.10.093.
- [35] S. CHEN, W. HUANG, J. ZHENG and Z. LI. Study on the electrodisolution and roughening of a palladium electrode in chloride containing solutions. *Journal of Electroanalytical Chemistry*, **660** (2011) 1 80. doi:10.1016/j.jelechem.2011.06.008.
- [36] L. FANG, Q. TAO, M.-F. LI, L. WEN LIAO, D. CHEN and Y. XIA CHEN. Determination of the real surface area of palladium electrode. *Chinese Journal of Chemical Physics*, **23** (2010) 5 543.
- [37] D. RAND and R. WOODS. The nature of adsorbed oxygen on rhodium, palladium and gold electrodes. *Journal of Electroanalytical Chemistry and Interfacial Electrochemistry*, **31** (1971) 1 29. doi:10.1016/S0022-0728(71)80039-6.

- [38] A. CORREIA, L. MASCARO, S. MACHADO and L. AVACA. Active surface area determination of Pd-Si alloys by H-adsorption. *Electrochimica Acta*, **42** (1997) 3 493. doi:10.1016/S0013-4686(96)00232-0.
- [39] Q. KONG, L. LIAN, Y. LIU, J. ZHANG, L. WANG and W. FENG. Bulk hierarchical nanoporous palladium prepared by dealloying pdal alloys and its electrochemical properties. *Microporous and Mesoporous Materials*, **208** (2015) 152. doi:10.1016/j.micromeso.2015.01.017.
- [40] Y. CAO, X. MA, Y. CHEN, G. SHAN and F. LIU. Size effect of ligaments on charge induced surface stress response of nanoporous Pd prepared by dealloying. *Scripta Materialia*, **123** (2016) 1. doi:10.1016/j.scriptamat.2016.05.040.
- [41] J. ERLEBACHER, M. J. AZIZ, A. KARMA, N. DIMITROV and K. SIERADZKI. Evolution of nanoporosity in dealloying. *Nature*, **410** (2001) 6827 450. doi:10.1038/35068529.
- [42] I. MCCUE, E. BENN, B. GASKEY and J. ERLEBACHER. Dealloying and dealloyed materials. *Annual Review of Materials Research*, **46** (2016) 1 263. doi:10.1146/annurev-matsci-070115-031739.
- [43] R. VISWANATH and J. WEISSMÜLLER. Electrocapillary coupling coefficients for hydrogen electrosorption on palladium. *Acta Materialia*, **61** (2013) 16 6301. doi:10.1016/j.actamat.2013.07.013.
- [44] Z. ZHANG, Y. WANG, Z. QI, C. SOMSEN, X. WANG and C. ZHAO. Fabrication and characterization of nanoporous gold composites through chemical dealloying of two phase al-au alloys. *J. Mater. Chem.*, **19** (2009) 6042. doi:10.1039/B904052H.
- [45] L. ISAEVA, D. BAZHANOV, E. ISAEV, S. EREMEEV, S. KULKOVA and I. ABRIKOSOV. Dynamic stability of palladium hydride: An ab initio study. *International Journal of Hydrogen Energy*, **36** (2011) 1 1254 . doi:10.1016/j.ijhydene.2010.06.130.
- [46] S. Y. ZAGINAICHENKO, Z. A. MATYSINA and D. V. SHCHUR. Statistical theory of forming structural vacancies in palladium hydride. *Russian Physics Journal*, **54** (2011) 2 199. doi:10.1007/s11182-011-9598-z.

- [47] M. HAKAMADA, T. FURUKAWA, T. YAMAMOTO, M. TAKAHASHI and M. MABUCHI. Abnormal hydrogen absorption/desorption properties of nanoporous Pt with large lattice strains. *MATERIALS TRANSACTIONS*, **52** (2011) 4 806. doi:10.2320/matertrans.M2010403.
- [48] M. GRDEŃ, J. KOTOWSKI and A. CZERWIŃSKI. Study of electrochemical palladium behavior by the quartz crystal microbalance. i. acidic solutions. *Journal of Solid State Electrochemistry*, **3** (1999) 6 348. doi:10.1007/s100080050165.
- [49] K. JUODKAZIS, J. JUODKAZYTĖ, B. ŠEBEKA, G. STALNIONIS and A. LUKINSKAS. Anodic dissolution of palladium in sulfuric acid: An electrochemical quartz crystal microbalance study. *Russian Journal of Electrochemistry*, **39** (2003) 9 954. doi:10.1023/A:1025724021078.
- [50] T. HONGO, K. EDALATI, H. IWAOKA, M. ARITA, J. MATSUDA, E. AKIBA and Z. HORITA. High-pressure torsion of palladium: Hydrogen-induced softening and plasticity in ultrafine grains and hydrogen-induced hardening and embrittlement in coarse grains. *Materials Science and Engineering: A*, **618** (2014) 1. doi:10.1016/j.msea.2014.08.074.
- [51] B. AMIN-AHMADI, D. CONNÉTABLE, M. FIVEL, D. TANGUY, R. DELMELLE, S. TURNER, L. MALET, S. GODET, T. PARDOEN, J. PROOST, D. SCHRYVERS and H. IDRISSE. Dislocation/hydrogen interaction mechanisms in hydrided nanocrystalline palladium films. *Acta Materialia*, **111** (2016) 253. doi:10.1016/j.actamat.2016.03.054.
- [52] P. SOFRONIS and H. BIRNBAUM. *Hydrogen enhanced localized plasticity: A mechanism for hydrogen related fracture*, volume 36, pages 15–25. Publ by ASME (1993).
- [53] E. DILLON, G. JIMENEZ, A. DAVIE, J. BULAK, S. NESBIT and A. CRAFT. Factors influencing the tensile strength, hardness, and ductility of hydrogen-cycled palladium. *Materials Science and Engineering: A*, **524** (2009) 1–2 89. doi:10.1016/j.msea.2009.07.036.
- [54] B. BAL, M. KOYAMA, G. GERSTEIN, H. MAIER and K. TSUZAKI. Effect of strain rate on hydrogen embrittlement susceptibility of twinning-induced plasticity steel pre-charged with high-pressure hydrogen gas. *International Journal of Hydrogen Energy*, **41** (2016) 34 15362. doi:10.1016/j.ijhydene.2016.06.259.

- [55] Y. MOMOTANI, A. SHIBATA, D. TERADA and N. TSUJI. Effect of strain rate on hydrogen embrittlement in low-carbon martensitic steel. *International Journal of Hydrogen Energy*, **42** (2017) 5 3371. doi:10.1016/j.ijhydene.2016.09.188.
- [56] A. CZERWIŃSKI, M. GRDEŃ and M. ŁUKASZEWSKI. Dual mechanism of hydrogen desorption from palladium alloys postulated on the basis of cyclic voltammetric studies. *Journal of Solid State Electrochemistry*, **8** (2004) 6 411. doi:10.1007/s10008-003-0448-y.
- [57] D. N. JEWETT and A. C. MAKRIDES. Diffusion of hydrogen through palladium and palladium-silver alloys. *Trans. Faraday Soc.*, **61** (1965) 932. doi:10.1039/TF9656100932.
- [58] B. BOYCE and M. DILMORE. The dynamic tensile behavior of tough, ultrahigh-strength steels at strain-rates from 0.0002 s<sup>-1</sup> to 200 s<sup>-1</sup>. *International Journal of Impact Engineering*, **36** (2009) 2 263. doi:10.1016/j.ijimpeng.2007.11.006.
- [59] M. SOARE and W. CURTIN. Single-mechanism rate theory for dynamic strain aging in fcc metals. *Acta Materialia*, **56** (2008) 15 4091. doi:10.1016/j.actamat.2008.04.030.
- [60] N. SCHUBERT, M. SCHNEIDER and A. MICHEALIS. The mechanism of anodic dissolution of cobalt in neutral and alkaline electrolyte at high current density. *Electrochimica Acta*, **113** (2013) 748. doi:10.1016/j.electacta.2013.06.093.
- [61] C. H. HAMANN and W. VIELSTICH. *Elektrochemie 4. Auflage*. WILEY-VCH (2005).
- [62] M. FISCHER, M. WERBER and P. V. SCHWARTZ. Batteries: Higher energy density than gasoline? *Energy Policy*, **37** (2009) 7 2639. doi:10.1016/j.enpol.2009.02.030.
- [63] A. ZÜTTEL. Materials for hydrogen storage. *Materials Today*, **6** (2003) 9 24. doi:10.1016/S1369-7021(03)00922-2.
- [64] J. REN, N. M. MUSYOKA, H. W. LANGMI, M. MATHE and S. LIAO. Current research trends and perspectives on materials-based hydrogen storage solutions: A critical review. *International Journal of Hydrogen Energy*, **42** (2017) 1 289. doi:10.1016/j.ijhydene.2016.11.195.



# Acknowledgements

At this point I would like to thank a few people who contributed to this master's thesis in one way or another.

**Univ.-Prof. Dr. Roland Würschum, Institute of Materials Physics, TU Graz**

For giving me the opportunity to write my master's thesis at the Institute of Materials Physics and supervising the project. His professionalism and experience in academic research improved this thesis to a great extent.

**Dr. Eva-Maria Steyskal, Institute of Materials Physics, TU Graz**

For her invaluable guidance in the first months of my work and countless discussions at later stages. Her helpful suggestions regarding experiments and explanations were greatly appreciated. The great degree of freedom given to me improved my understanding of the subject widely.

**Priv.-Doz. Dr. Peter Pölt, Institute of Electron Microscopy and Nanoanalysis, TU Graz**

For giving me the possibility to characterise nanoporous palladium via scanning electron microscopy.

**Dipl.-Ing. Tobias Achtsnit and Sanja Simic, Institute of Electron Microscopy and Nanoanalysis, TU Graz**

For their time conducting the SEM investigations and the electron micrographs obtained.

**Assoc. Prof. Norbert Enzinger, Dipl.-Ing. Christopher Wiednig and Dipl.-Ing. Markus Stütz, Institute of Materials Science, Joining and Forming**

For carefully preparing the cobalt palladium alloys via electron beam melting (EBM), which enabled the systematic study of the dealloying process and different nanoporous samples.

**Dipl.-Ing. Gregor Klinser, Institute of Materials Physics, TU Graz**

For his kind help in solving many smaller issues in the lab or elsewhere.

**My colleagues at the Institute of Materials Physics, TU Graz**

For all their support and making every day at the office enjoyable.

**My fellow physics students and friends**

For Thursday lunchtime and several coffee breaks spent together, in discussion or friendly chat.

**My family**

For their wide and ongoing support during my studies, their patience and encouragement at any moment.